Multidimensional Fourier spectroscopy of semiconductors. II. Decoherence effects

Kuljit S. Virk* and J. E. Sipe†
Department of Physics and Institute for Optical Sciences, University of Toronto, 60 St. George Street, Toronto, Ontario, Canada M5S 1A7

(Received 6 July 2009; revised manuscript received 26 August 2009; published 15 October 2009)

We study decoherence between the states of optically excited excitons embedded in an electron gas and compare it to the decoherence between the excitons and the ground state. The problem is examined within the context of two-dimensional Fourier spectroscopy using the formalism discussed in the first paper of this series [K. S. Virk and J. E. Sipe, Phys. Rev. B **80**, 165318 (2009)]. Two-time correlation functions for excitons are constructed and a dynamical equation describing their evolution is derived. The equation is compared to the corresponding equation for the interband polarization. It is argued, and verified by numerical calculation, that the decay of *Raman coherence* between exciton states is much slower than the decay of interband polarization and that it depends explicitly on how differently the superimposed exciton states interact with modes of the electron gas. The equations are generally non-Markov. Numerical results are obtained for a simple model of low-energy excitations of a GaAs quantum well.

DOI: 10.1103/PhysRevB.80.165319 PACS number(s): 78.47.−p, 71.35.−y, 42.50.Md, 78.67.−n

I. INTRODUCTION

Decoherence forms an important part of the dynamics of electrons in semiconductors at ultrafast time scales. The coherent optical excitation of a semiconductor induces a superposition of many-body states, which eventually decays due to interactions. The interference resulting from this coherence is an important feature of four-wave mixing experiments,[1] plays a central role in the generation of current and photon echos,[2–6] and has been exploited to optically inject charge and spin currents.[7,8] More recently, the technique of multidimensional Fourier spectroscopy has been successfully applied to semiconductor quantum wells[9–11] and has already proved useful in identifying the effects of decoherence on signals generated by the laser-semiconductor interaction.

In the first paper[12] of this series, hereafter referred to as I, we presented a formalism that uses nonequilibrium Green's functions to model three-pulse excitation of semiconductors. The formalism is general enough to handle a variety of initial states, including a quasiequilibrium distribution of carriers established prior to the excitation. We also developed a diagram method that is useful in analyzing the many-body interactions and optical excitation on an equal footing. In this paper, we complement the abstract nature of paper (I) by applying the formalism to a specific problem: the decoherence of exciton states in a background electron gas. We focus on systems in which the hole and exciton densities prior to optical excitation densities are vanishing.

The argument for studying this problem is threefold. First, excitons are arguably the most experimentally accessible many-body states. Second, exciton states represent the simplest many-body excitations that can be used as a concrete example for testing any formalism. Third, their interaction with an electron gas presents a new regime of decoherence, where the usual system-bath separation does not exist owing to the indistinguishability of the electron in the exciton from that in the gas. In this paper, we show that, at least within a physically motivated set of approximations, decoherence effects in this scenario can be brought into direct comparison to the conventional system-bath models while respecting the indistinguishability.

In studying the dynamics of optically excited excitons, the specific property of interest is *Raman coherence*.[13] Raman coherence refers to the coherence between excited states of the semiconductor. Being a coherence between excited states, it is not directly injected by linear optical excitation, in contrast to interband polarization, which is a coherence between the ground state and an excited state. Raman coherences can be dominated by the exchange and correlation in the multiparticle states and can thus be fundamentally different from the mere beating of interband coherences. The formalism that we apply in the present paper is built to handle precisely this exchange-correlation part and we quantify the extent to which the exchange and correlation dominate. Nonetheless, it is the beating of interband coherences that gives rise to a driving term, which leads to the rise of coherences in multiparticle correlations. The first major result of the present paper is the microscopic description of one such mechanism of this *transfer* of coherence.

The mechanism in question is driven by the dynamical response of the electron gas, more precisely the density-density correlation. This response leads to a nonfactorizable correlation among two interband polarization amplitudes. At the same time, the continuum of excitations in the electron gas, consisting of plasmons and pair excitations, leads to a "measurement" of this coherence. The same dynamical response thus also leads to the diminishing of the coherence it helps build. Yet the two processes do not cancel. While the appearance of this coherence originates from the strength of the multipole moments of the two exciton states, the decoherence depends *sensitively* on how differently the two multipoles interact with the electron gas. Incidentally, this is also the origin of decoherence in traditional models where different system states scatter a bath state into two different states with vanishing overlap. The reasoning applies also to the interband coherence, which is a superposition of the presence and absence of exciton. In terms of scattering, the two states are distinguished by any scattering event. The second major result of the paper is the explicit analytical and numerical demonstration of these facts. We find that exciton states with similar momentum space profiles tend to have Raman coher-

ences that far outlive their respective coherences with the ground state.

Furthermore, an exciton is a composite particle, consisting of an electron and a hole. In the limit of low density of the surrounding electron gas, the composite nature of the exciton can largely be ignored. However, as the density rises, the electron and hole, besides being bound to each other, can *individually* interact with the electrons in the gas. This interaction includes not only the Coulomb interaction but also the exchange interaction, since the electrons in the gas can be exchanged with that bound to the hole. It then becomes necessary to take into account these new effects in describing the dynamics of excitons embedded in an electron gas.

This brings us to the third major result of the paper. We find that the dynamical equations for the excitons involve two classes of functions: those that treat exciton as indivisible and thus are sensitive only to its multipole moments and those that treat exciton as a composite particle and take into account the individual propagation of the electron and the hole. The latter is connected to excitations of the N-particle many-body system in the $N\pm 1$-particle Hilbert space. We find that for densities involved for our choice of material parameters, the composite nature of the exciton makes little contribution. Therefore, we ignore it in our analysis, but its appearance in the equations will be useful for future analyses in different parameter regimes.

In the calculations described below, we first study the exciton levels in the presence of static screening. The screening originates from the conduction-band electrons that are assumed to be present in the samples via doping and we take the hole and exciton densities to be equal to zero in the initial quasiequilibrium state. The screening is controlled by a single parameter, which is calculated self-consistently for a fixed density of the electron gas. For at least three bound exciton states to exist, we find that a density lower than an electron per exciton radius is required. We study decoherence between $2s$ and $2p$ states, neglecting spin as well as anisotropy of energy bands.

This paper is organized as follows. In Sec. II, we begin by establishing the link between our approach and the more conventional descriptions based on wave functions or density matrices. We then discuss the relevance of our theoretical approach, and the calculations we make, to signals that can be observed in two-dimensional Fourier spectroscopy (TDFS) experiments. In Sec. III, we present the equations of motion for our dynamical quantities and a discussion of the nature of the approximations made. The dynamics governed by the equations of motion is analyzed in Sec. IV, where we present and analyze the dynamics in a way that makes the three results sketched above analytically explicit. In Sec. V, we discuss our numerical technique for solving the two-time non-Markov equations, as well as the model for the electron gas we have used in our calculations. In Sec. VI, we present results of three different calculations and discuss them in the context of our analysis of the dynamical model; our conclusions are presented in Sec. VII. For some of the quantities introduced as part of the general formalism in I, but which appear often in this paper, it is convenient to adopt a shorthand notation here. In Appendix A, we include some technical definitions and a table listing the key theoretical quantities in both the general and the shorthand notations, their physical significance, and references to defining equations. Some details of calculations are also relegated to Appendixes B and C. In Appendix B, we discuss our approximation method to restrict four-point functions to depend only on two time variables. In Appendix C, Sec. C 1, we discuss the derivation of the equation of motion (EOM) for the exciton correlation function, and in Appendix C, Sec. C 2, we discuss the similar derivation for the interband polarization.

II. BACKGROUND

A. Conceptual motivation

In this section, we discuss various types of coherences and the issues related to them on formal grounds. In particular, we begin with a traditional wave-function perspective to identify the two main types of coherences that are accessible optically in semiconductors. We then recast them in the Green's function language and point out the important physical aspects of the dynamics of these coherences that can be handled naturally within our formalism.

Consider an optical excitation of a quantum well close to its band-gap energy with a pulse so weak that the dominant effect is the generation of an interband polarization. In the independent-particle approximation, we can describe the state of the system as

$$|\psi(t)\rangle \propto |\Phi_0\rangle + \sum_{\boldsymbol{k}} \alpha_{cv\boldsymbol{k}}(t)|cv,\boldsymbol{k}\rangle,$$

where $|\Phi_0\rangle$ is the ground state of the system and $|cv,\boldsymbol{k}\rangle$ is a state with a conduction electron and a valence hole. The amplitudes $\alpha_{cv\boldsymbol{k}}(t)$ are proportional to the dipole matrix elements and the electric field. In a perfectly coherent system, the unitary evolution of this state is fully captured by the amplitudes $\alpha_{cv\boldsymbol{k}}(t)$. To step beyond this regime, we write the corresponding density matrix

$$\varrho(t) \propto |\Phi_0\rangle\langle\Phi_0| + \sum_{\boldsymbol{k}} [\alpha_{cv\boldsymbol{k}}(t)|cv,\boldsymbol{k}\rangle\langle\Phi_0| - \alpha^*_{cv\boldsymbol{k}}(t)|\Phi_0\rangle\langle cv,\boldsymbol{k}|] + \sum_{\boldsymbol{k}\boldsymbol{k}'} \alpha_{cv\boldsymbol{k}}(t)\alpha^*_{cv\boldsymbol{k}'}(t)|cv,\boldsymbol{k}\rangle\langle cv,\boldsymbol{k}'|. \quad (1)$$

Here we interpret the second term as a coherence between the ground state and an excited state containing one electron-hole pair. It arises from the superposition between existence and nonexistence of the electron-hole pair. The third term describes another superposition, in which both states involved contain an electron-hole pair but in different states of the two-particle Hilbert space. These are often referred to as *Raman* coherences.[13] In other words, the second term is a coherence between two different Hilbert spaces (namely, zero and two-particle), while the third term is a coherence within a single Hilbert space.

We can abstract from this perspective a more general expression for $\varrho(t)$ in the form

$$\varrho(t) \propto |\Phi_0\rangle\langle\Phi_0| + \varrho_1(t) + \varrho_2(t). \quad (2)$$

Elements of $\varrho_1(t)$ are coherences between the ground state and the excited states (interband coherences) and those of

$\varrho_2(t)$ are coherences among the excited states (intraband coherences). While their relationship is fixed by Eq. (1) within the noninteracting particle picture, their evolution can be dramatically different when interactions are taken into account. When interactions are present, of course, the very idea of a "single-particle state" loses its validity. Nonetheless, at short-enough time scales, the concepts of quasiparticle bands and crystal momentum retain an approximate validity. This "quasiparticle regime" is discussed, within our approach, in Sec. IV of I. It is an underlying assumption in the present calculation that this quasiparticle regime extends to picosecond time scales.

We now turn to a Green's function description of the scenario of Eq. (1). Very generally, the single and two-particle Green's functions are defined as

$$G(12) = -i\langle \mathcal{T}_C a(1)a^\dagger(2)\rangle, \tag{3}$$

$$G(14;23) = -\langle \mathcal{T}_C a(1)a(4)a^\dagger(3)a^\dagger(2)\rangle, \tag{4}$$

in the (standard) notation of I; a and $a^\dagger$ are, respectively, annihilation and creation operators and indices such as 1 can be taken to label a space and time point, or alternately an index of a nominal band and a crystal momentum, together with a time. A usual decomposition of $G(14;23)$ is

$$G(14;23) = G(12)G(43) - X^{(2)}(14';23'), \tag{5}$$

where the first term alone is the *Hartree* approximation and the second is a correction that accounts for *exchange* and *correlation*; the second term is written in notation of I.[14] In a semiconductor, once the conduction (c) and valence (v) bands have been identified, the interband coherences ($\alpha_{cv\mathbf{k}}$) arising in the simple description [Eqs. (1) and (2)] are described in the Green's function formalism by the equal-time limit of the component

$$G_{cv}(12) = -i\langle \mathcal{T}_C a_c(1)a_v^\dagger(2)\rangle$$

of the Green's function (3). Here, we explicitly display the bands associated with the indices (c with 1 and v with 2) and the indices themselves only indicate a crystal momentum and time. The quasiequilibrium background state is subjected to the condition $G_{cv}(12)=0$, which means that no coherence exists in the system prior to optical excitation. The two-particle propagation involved in exciton states is handled by a component of the four-point Green's function (4) in which one electron resides in the conduction and one in valence band

$$G_{cvvc}(14;23) = -\langle \mathcal{T}_C a_c(1)a_v(4)a_c^\dagger(3)a_v^\dagger(2)\rangle.$$

This Green's function describes the propagation of two electrons, added to the system at times t_2 and t_3, and subsequent removal at times t_1 and t_2, respectively. The equal-time limit ($t_2=t_1\equiv t$, $t_4=t_3=t_1^+$) describes the coherences that are given by $\alpha_{cv\mathbf{k}}(t)\alpha^*_{cv\mathbf{k}'}(t)$ in the simple description [Eqs. (1) and (2)]. More generally,

$$G_{cvvc}(14;1^+4^+) = G_{cv}(11^+)G_{vc}(44^+) - X^{(2)}_{cvvc}(14;1^+4^+), \tag{6}$$

where $G_{cv}(11^+)$ describes the interband coherence. In the equal-time limit and with interactions turned off,

$$G_{cvvc}(\mathbf{k}_a t,\mathbf{k}_d t;\mathbf{k}_b t^+,\mathbf{k}_c t^+) = G_{cv}(\mathbf{k}_a t,\mathbf{k}_b t^+)G_{vc}(\mathbf{k}_d t,\mathbf{k}_c t^+) - G_{cc}(\mathbf{k}_a t,\mathbf{k}_c t^+)G_{vv}(\mathbf{k}_d t,\mathbf{k}_b t^+). \tag{7}$$

Comparing Eq. (7) to the product $\alpha_{cv\mathbf{k}}(t)\alpha^*_{cv\mathbf{k}'}(t)$ and recalling Eq. (1), it becomes clear that a wave-function description is possible only if the carrier density can be ignored so that the exchange interaction among electrons is negligible. The second term in the last equation represents the effect of indistinguishability of electrons that prevents one from treating an electron-hole pair as a closed system in the presence of electron gas, even with all interactions turned off. If the Coulomb interactions are allowed but $G_{cc}(\mathbf{k}_a t,\mathbf{k}_c t^+)\approx 0$, then they bind electron and hole into an exciton that can be treated as a particle in the semiconductor vacuum.

Further interactions also screen the Coulomb interaction via the response of the medium surrounding the exciton. If that response is such that the screening is effectively static, then $G_{cvvc}(\mathbf{k}_a t,\mathbf{k}_d t;\mathbf{k}_b t^+,\mathbf{k}_c t^+)\approx G_{cv}(\mathbf{k}_a t,\mathbf{k}_b t^+)G_{vc}(\mathbf{k}_d t,\mathbf{k}_c t^+)$ continues to hold, but the exciton states associated with the poles of the two-particle Green's function will be modified. If the dynamic nature of the response is taken into account, then correlations between the screening medium and the exciton will contribute to $X^{(2)}$, thus destroying a wave-function description of the state of the system. So we see that in general, there are two reasons why it is impossible to maintain Eq. (1) as the state of the system: the presence of exchange interaction and the presence of interaction with a surrounding medium including electrons.

In following the excitation of the system by optical fields, we track the deviations induced in the original, quasiequilibrium $X^{(1)}\equiv G$ and $X^{(2)}$. The deviations at order n in the effective field, U, are identified by the functions $\mathfrak{X}_n^{(1)}$ and $\mathfrak{X}_n^{(2)}$ with additional subscripts indicating bands. With some caveats, U, can be identified as the optical perturbation driving transitions between the valence and conduction bands.[12,15] At $n=2$, $\mathfrak{X}^{(2)}_{2;cvvc}$ will contribute significantly to G_{cvvc}. At frequencies corresponding to the exciton states, the optically generated densities may indeed be small and the dominant correction will arise mainly from dynamical interactions. The purely exchange term will be important if the coupling between exciton dynamics and the optically injected electron and hole densities is large.

The dynamical interactions will drive the system toward a new quasiequilibrium state involving excited electron-hole pairs, electron gas, and other quasiparticles, such as phonons, that may be important. Since it is a good approximation to neglect any interband transitions via Coulomb interaction, this quasiequilibrium state will be devoid of any interband polarization, i.e., $G_{cv}\to 0$. Thus, as the system moves from an initial excitation of interband coherence to quasiequilibrium, the functions $\mathfrak{X}^{(2)}_{cvvc}$ entirely take over the contribution to the two-particle states of the system. Furthermore, when

bound excitons can be formed, the dynamics of $\mathfrak{X}^{(2)}_{cvvc}$ is much richer than the dynamics of G_{cv} alone. This is because the decay of G_{cv} is sensitive to any scattering event involving the excited pair, while the decay of $\mathfrak{X}^{(2)}_{cvvc}$ is sensitive to *how different* are the scattering properties of the two superimposed states. This point becomes explicit in the equations of motion we introduce below for the two objects, which can be compared on an equal footing.

We also remark that both the rise of coherence in $\mathfrak{X}^{(2)}_{cvvc}$ associated with the optical excitation and the subsequent decoherence are mediated by dynamical interactions. Neglecting phonons, as we do in this paper, these dynamical interactions in turn require that the density-density correlation in the many-body electronic system is nonzero, i.e.,

$$X^{(2)}(\boldsymbol{r}t,\boldsymbol{r}'t';\boldsymbol{r}t^{+}\boldsymbol{r}'t'^{+}) = \langle \hat{n}(\boldsymbol{r},t)\hat{n}(\boldsymbol{r}',t')\rangle - \langle \hat{n}(\boldsymbol{r},t)\rangle\langle \hat{n}(\boldsymbol{r}',t')\rangle \neq 0,$$

where $\hat{n}(\boldsymbol{r},t)$ is the electron-density operator. In the original quasiequilibrium state, we associate this fluctuation with the quasiparticle density in the partially filled conduction band and treat the filled valence bands as inert. Fluctuations in the semiconductor vacuum must involve the formation of virtual electron-hole pairs with energy close to the fundamental gap and therefore they are very short lived. Only the much longer time scale of fluctuations of the gas formed in the conduction band is of relevance in this work. The role of dynamical interactions in both coherence and decoherence will also be seen explicitly below when comparing the dynamical map for $\mathfrak{X}^{(2)}$ to the source terms driving it.

Thus we see that it is natural to study the decoherence of excitons using only the function $\mathfrak{X}^{(2)}_{cvvc}$, which is free of the short-lived contributions of interband polarization to the total two-particle Green's functions. As functions of four arguments, these are too large for computation and describe far more effects than we aim to capture in this work. In the following section, we will describe a set of approximations that restricts these functions to describe excitons in a way similar to quasiparticles, while being sensitive to their composite nature as well.

B. Relationship to experiment

The main quantity studied in this paper is the two-particle correlation function for excitons and the main property of this function that we focus on is Raman coherence. In this section, we discuss how this quantity is related to experimentally measurable signals. For concreteness, we pick the exciton states $2s$ and $2p$, which lie within a few meV of the conduction-band edge for the electron density involved. The $2s$ state is excited by single-photon absorption while the $2p$ state is excited by two-photon absorption. We assume that the first two pulses in the excitation sequence are coincident and predominantly excite these states. This restriction on excitations holds for optical frequencies that resonate with excitation from the ground state to exciton states. At much lower frequencies, field-driven transitions from exciton to higher-particle correlations may become important, but they can be safely ignored here. We are not interested in the dynamics with respect to the delay between the first and the second pulses and have thus taken the pulses to be overlapping in time. This minimizes the effects of first-order deviations in multiparticle correlations, such that the coherence between two-particle states is driven mainly by interband polarization only. We let the third pulse arrive a time t_d after the first two pulses and we let τ be the time after the third pulse when the signal is detected. The process is illustrated diagrammatically in Fig. 11 of I. Henceforth, we will refer to equations and figures of Virk and Sipe[12] (I) as "I-" followed by the corresponding number in that paper.

As discussed in Sec. I-IVC, the electromagnetic signal corresponding to TDFS for this scenario is given by the current density I-(115),

$$\langle \boldsymbol{J}_3(\boldsymbol{q}|t)\rangle = -e\,\delta(\boldsymbol{q}-\boldsymbol{k}_1+\boldsymbol{k}_2-\boldsymbol{k}_3)\int \frac{d\boldsymbol{k}}{4\pi^2}\omega_{cv}(\boldsymbol{k})\boldsymbol{\xi}_{vc}(\boldsymbol{k})\mathfrak{X}^{(1)}_{3;cv} \times(\boldsymbol{k}t;\boldsymbol{k}t^{+}) + \text{c.c.}, \tag{8}$$

where $\boldsymbol{\xi}_{vc}(\boldsymbol{k})$ is the matrix element of the position operator, $\omega_{cv}(\boldsymbol{k})=[E_c(\boldsymbol{k})-E_v(\boldsymbol{k})]/\hbar$, where E_c and E_v are the conduction and valence-band energies, and $\mathfrak{X}^{(1)}_{3;cv}$ is the third-order deviation (in the effective field) in the single-particle Green's function. In the following, we set $\omega_{cv}(\boldsymbol{k})$ equal to the fundamental gap frequency, ω_g, and neglect the small contribution arising from its dependence on $\boldsymbol{k}$. We estimate $\mathfrak{X}^{(1)}_{3;cv}$ by its source terms alone and ignore the convolution effects of the decoherence causing terms in this interband polarization (see I).

There are two contributions to the third-order interband polarization, as shown in Fig. I-11. The first arises from the Pauli blocking due to the optically injected carriers and the second due to the Raman coherence of exciton states. It is the second contribution that is of primary interest to us in this paper and it appears in a different region of two-dimensional spectrum than the former. Thus we study only this contribution. To indicate that only the exciton contribution is included, we put the superscript "ex" on $\boldsymbol{J}_3$.

Based on the above approximations and substituting I-(110) in I-(115), we obtain

$$\langle \boldsymbol{J}^{ex}_3(\boldsymbol{q};t_d,\tau)\rangle = -e\,\delta(\boldsymbol{q}-\boldsymbol{k}_1+\boldsymbol{k}_2-\boldsymbol{k}_3)\omega_g\sum_n \boldsymbol{d}_{mn}\tilde{\mathcal{P}}_{nm}\left(t_d+\frac{\tau}{2},\tau\right) \times e^{-i\omega_{nm}t_d}e^{-i\omega_n\tau/2} + \text{c.c.} \tag{9}$$

Here, the vector coefficients $\boldsymbol{d}_{mn}$ are given by the projection of optical transition matrix elements onto the exciton states. The arguments t_d and τ correspond to the delays between the first two and the third pulse and between the third pulse and the time of measurement, respectively. The function $\tilde{\mathcal{P}}(t,\tau)$ is the exciton correlation function of second order in the effective field. It is the exchange-correlation part of the exciton Green's function that gives an amplitude for the system with an exciton removed from state m at time t_d to evolve into the state with an exciton removed from level n at time $t_d+\tau/2$. It is also a restricted form of the more general correlation functions, $\mathfrak{X}^{(2)}_{2;cvvc}$, of the formalism of I.[16] When the radiated electromagnetic field is calculated from this current density, there are additional effects arising from the propagation inside the well and radiation reaction and their treatment is

discussed at length in Appendix IA. We do not consider them in this paper.

Due to the dependence of the right-hand side of Eq. (9) on t_d and τ, $\langle \boldsymbol{J}_3^{ex} \rangle$ also becomes a function of these two variables. The two-dimensional Fourier transform of the signal with respect to the two time delays is then given by

$$\langle \boldsymbol{J}_3^{ex}(\boldsymbol{q};\omega,\Omega)\rangle = -e\,\delta(\boldsymbol{q}-\boldsymbol{k}_1+\boldsymbol{k}_2-\boldsymbol{k}_3)\omega_{cv}(\boldsymbol{0}) \times \sum_{nm} \boldsymbol{d}_{mn}\tilde{\mathcal{P}}_{nm}\left(\omega-\omega_{nm},\Omega-\frac{\omega}{2}-\frac{\omega_n+\omega_m}{2}\right), \tag{10}$$

where $\tilde{\mathcal{P}}_{nm}(\omega,\Omega)$ is the two-dimensional Fourier transform of $\tilde{\mathcal{P}}_{nm}(t,\tau)$. Thus the signal can also be viewed as the transfer of Raman coherence back to interband coherence, which radiates at optical frequencies.

The two-dimensional spectrum in Eq. (10) is a sum of the matrix elements $\tilde{\mathcal{P}}_{nm}(\omega,\Omega)$ and in the numerical calculations the dominant matrix elements are those between the $2s$ and $2p$ states. The different components $\tilde{\mathcal{P}}_{nm}(\omega,\Omega)$ appear as peaks in different parts of the two-dimensional spectrum. Furthermore, we show in Sec. III A 2 that, at least under the assumption of isotropic bands, $\tilde{\mathcal{P}}_{nm}(\omega,\Omega)$ and $\tilde{\mathcal{P}}_{mn}(\omega,\Omega)$ lead to radiation in different directions. Therefore, when presenting results in Sec. VI, we plot the functions $\tilde{\mathcal{P}}_{nm}(\omega,\Omega)$.

The pulse sequence is such that only the beating of the interband polarizations appears in the two-dimensional spectrum. However each interband polarization also emits a signal. Though it may be difficult to detect, it is nonetheless related directly to the projection of $\mathfrak{X}_{1;cv}^{(1)}(11^+)$ onto the exciton basis. In the equations below, we write this $O(U)$ deviation in single-particle density matrix as

$$\rho(1) \equiv -i\mathfrak{X}_{1;cv}^{(1)}(11^+). \tag{11}$$

III. EQUATIONS OF MOTION

A. From general formalism to specific model

It is clear from the discussion in the previous section that the results of measurements in the parameter regime of interest are sensitive primarily to the single and two-particle correlations, $\mathfrak{X}_1^{(1)}$ and $\mathfrak{X}_2^{(2)}$. As discussed at length in I, these functions are part of a generalized susceptibility expansion, which is a response to the effective field inside the semiconductor. These functions have components labeled by both the band indices and sometimes the Keldysh contour branch indices, which we denote by superscripts + and −. The important component of the function $\mathfrak{X}_1^{(1)}$ is the interband polarization, while the important component of $\mathfrak{X}_2^{(2)}$ is the exchange-correlation part of the electron-hole propagation. Naturally, these functions are coupled to the rest of their own components and to functions of different order in both particle number and the effective field. These couplings are through effective interactions for which models must be specified. The remaining part of Sec. II is devoted to this and the key quantities that arise in construction of the models are listed in Table I.

The formal structure of the equations of motion is given in Eqs. I-(63)–I-(68), which we now apply to the present problem. While the formalism in I identifies many-body contributions in full generality to the third order in the driving field, in a particular application only a few of those contributions may be of interest. In this section, we identify the relevant contributions based on the fact that the density of electron gas is less than one electron per exciton radius.

The equations for the two functions, $\mathfrak{X}_1^{(1)}$ and $\mathfrak{X}_2^{(2)}$, are reproduced here for easy reference

$$i\frac{\partial}{\partial t_j}\mathfrak{X}_1^{(1)}(12) = \mathcal{M}_1^{(11;j)}\mathfrak{X}_1^{(1)} + \mathcal{M}_1^{(12;j)}\mathfrak{X}_1^{(2)} + \mathcal{S}_1^{(1;j)}, \tag{12}$$

$$i\frac{\partial}{\partial t_j}\mathfrak{X}_2^{(2)}(14;23) = \mathcal{M}_2^{(21;j)}\mathfrak{X}_2^{(1)} + \mathcal{M}_2^{(22;j)}\mathfrak{X}_2^{(2)} + \mathcal{S}_2^{(2;j)}. \tag{13}$$

Here, j corresponds to the argument of the function being differentiated. There are two kinds of terms: $\mathcal{M}_n^{(ab;j)}$ are the couplings and $\mathcal{S}_n^{(i;j)}$ are the sources or driving terms. In the next two sections, we derive expressions for those.

1. Dynamical couplings

Equation (12) contains coupling to the function $\mathfrak{X}_1^{(2)}$. Within the low-density regime, this coupling, $\mathcal{M}_1^{(12;j)}$, can be subsumed into $\mathcal{M}_1^{(11;j)}$ [see Eqs. (C4) and (C5)]. In Eq. (13), $\mathcal{M}_2^{(21;j)}$ couples $\mathfrak{X}_2^{(2)}$ to the function $\mathfrak{X}_2^{(1)}$, which in the two-band model we adopt is identified with electron and hole densities. This coupling, along with Eq. (I-66) for $\mathfrak{X}_2^{(1)}$, describes effects of excitation induced carrier density on the dynamics of excitons; $\mathcal{M}_2^{(21;j)}$ also describes contributions to excitation-induced dephasing (EID), which corresponds to a partial resummation to all orders in the field. This is not the topic of the present paper.[17] At strictly second order in the electric field, one can verify that the coupling term $\mathcal{M}_2^{(21;j)}$ has one higher factor of electron density compared to $\mathcal{M}_2^{(22;j)}$. This is due to the vanishing hole and exciton densities in the background state.[18] Therefore, we drop this coupling in the following.

So we only need the couplings $\mathcal{M}_1^{(11;j)}$ and $\mathcal{M}_2^{(22;j)}$. The coupling $\mathcal{M}_1^{(11;j)}$ is given by I-(69) and I-(71)–I-(74) and $\mathcal{M}_2^{(22;j)}$ by I-(82), I-(85), I-(88), I-(89), and (I-92). In practice, $\mathcal{M}_1^{(11;j)}$ is obtained from the same derivation as $\mathcal{M}_2^{(22;j)}$ by demanding consistency in the approximations to many-body physics in Eqs. (12) and (13); explicit steps are given in Appendix C, Sec. C 2.

Our remaining task is to determine $\mathcal{M}_2^{(22;j)}$. Here, we necessarily rely heavily on the development in I and use the notation introduced and defined there. The remainder of this section is thus unavoidably formal; the final result is given in Eqs. (21)–(23).

We begin by writing $\mathcal{M}_2^{(22;1)}\mathfrak{X}_2^{(2)}$ in the expanded form using I-(71),

TABLE I. List of symbols for key theoretical quantities.

Notation of I[a]	This paper	Eqs.	Description
$\langle \boldsymbol{J}_3^{ex} \rangle$		9	Contribution of exciton correlations to the total current density.
$\mathfrak{X}_{3;cv}^{(1)}$		8	Third-order interband polarization.
$\tilde{\mathcal{P}}_{nm}(t_d,\tau)$		9	A component of exciton correlation function in $\langle \boldsymbol{J}_3^{ex} \rangle$. $\tilde{\mathcal{P}}_{nm}(t_d,\tau)=\mathcal{P}_{nm}^{<}(t_d+\tau,t_d)$. See below for $\mathcal{P}_{nm}^{<}$.
$\tilde{\mathcal{P}}_{nm}(\omega,\Omega)$		10	Fourier transform of $\tilde{\mathcal{P}}(t,\tau)$. The function plotted in the TDFS plots.
$W(14;23)$	$W_{\mathbb{Q}}^{\lessgtr}(\tau)$	A1	Dynamically screened interaction. Always evaluated at equilibrium in this paper.
$\mathfrak{X}_{1;cv}^{(1)+-}(11^+)$	$i\rho(1)$, $i\rho_{\boldsymbol{q}n}(t_1)$	11,25	Interband polarization at $O(U)$. The second form is the projection onto exciton basis. It also drives the Raman coherence for exciton correlations (see below). Quantity characterizing coherence between ground and exciton states.
$\mathfrak{X}_{2;cvvc}^{(2)+-+-}(12;1^+2^+)$	$\mathcal{P}^{<}(t_1,t_2)$	B4	Correlation function for an exciton in the two-time limit at $O(U^2)$. Quantity characterizing exchange-correlation contribution to Raman coherence.
$\mathfrak{X}_{2;cvvc}^{(2)-+-+}(12;1^+2^+)$	$\mathcal{P}^{>}(t_1,t_2)$	B4	Correlation function for an exciton in the two-time limit at $O(U^2)$ with reverse ordering of operators compared to $\mathcal{P}^{<}$.
$J_{cvvc}^{(2)+-+-}(12;1^+2^+)$	$\mathcal{J}^{<}(t_1,t_2)$	16	Component of the effective potential for the EOM for excitons. It is a functional of $W^{<}$ and $\mathcal{P}^{<}$.
$J_{cvvc}^{(2)-+-+}(12;1^+2^+)$	$\mathcal{J}^{>}(t_1,t_2)$	16	Component of the effective potential for the EOM for excitons. It is a functional of $W^{>}$ and $\mathcal{P}^{>}$.
$\mathcal{S}_{2;cvvc}^{(2;l)+-+-}(14;23)$	$\mathcal{S}_{\boldsymbol{q},nm}^{(2;l)}(t_1,t_2)$	31,32	Source term driving the exciton correlation $\mathcal{P}^{<}$ for external vertex l. The form in the second column corresponds to projection onto the exciton basis. It is generated by $\rho_{\boldsymbol{q}n}(t)$ defined above.
	$\mathcal{Q}(t)$	54	A phenomenological characterization of the nature of exchange-correlation in Raman coherences.

[a]Reference 12.

$$\mathcal{M}_2^{(22;1)}\mathfrak{X}_2^{(2)} = H(1)\delta(11')\mathfrak{X}_2^{(2)}(1'4;23) + [\Sigma_{\mathbb{Q}}(11')\delta(22') + G_{\mathbb{Q}}(2''2)I_{\mathbb{Q}}^{(2)}(12';2''1')]\mathfrak{X}_2^{(2)}(1'4;2'3) + \mathcal{K}^{(22;1)}(14;23|1'4';2'3')\mathfrak{X}_2^{(2)}(1'4';2'3'), \tag{14}$$

where the quantities on the right-hand side are defined in I; we note that the subscript "$\mathbb{Q}$" denotes evaluation in the quasiequilibrium state. The above equation, and the expression for $\mathcal{K}^{(22;1)}$ given by I-(85), shows that the only effective interaction needed is $I^{(2)}$.[19] We use our particular approximation scheme for $I^{(2)}$ to transform this expression into a simpler one that depends only on $X^{(2)}$ and the dynamical interaction $W_{\mathbb{Q}}$.

We mention only the key points involved in the derivation of the effective interaction $I^{(2)}$ and leave the algebraic manipulations elsewhere.[20] We neglect optically induced carrier densities in comparison to the background electron gas, which is what simplifies the interaction to just a function of $X^{(2)}$ and $W_{\mathbb{Q}}$. We obtain $I^{(2)}$ by restricting the three-time functions such that they are a product of fully interacting two-particle propagation and an independent propagation of the remaining quasiparticle after one of them is destroyed. This approximation yields an effective two-particle interaction $I^{(2)}$ that depends only on two times. Transforming four-point function that depends on three times into those that depend on two times is a common objective of the various approximations made in this section. In this regard, we give the general definition we have adopted for the two-time limit of a four-point function

$$F(tt') \equiv \lim_{t_1\to t}\lim_{t_2\to t'}\lim_{t_2\to t_1^+}\lim_{t_3\to t_4^+} F(14;23) = F(14;1^+4^+). \tag{15}$$

The limits in Eq. (15) apply only to the value of the time variable; the two branch indices of the Keldysh contour are still arbitrary. As shown in Appendix B, when Eq. (15) is applied to the Green's function, G_{cvvc}, the branch indices yield a 4×4 matrix in the Keldysh space with six different functions that have a clear physical interpretation. The ap-

proximation employed is also convenient in computation since it closes the dynamical equations within a set of two-time functions.

The other key technical points are rooted in the relatively low density of the electron gas. In this limit, excitations in the valence band are predominantly holelike and those in the conduction band are particlelike. The mathematical consequences of this are discussed in Sec. III B. In the limit of low density of optically injected carriers, the equation for $\mathfrak{X}^{(2)}_{cvvc}$ also decouples from the equation for G, which is equivalent to neglecting the coupling $\mathcal{M}^{(21;j)}_2$ in Eq. (13) and yields a simpler effective interaction that acts like a two-time potential in the equation for $\mathfrak{X}^{(2)}$. Higher-level approximations would consist of picking higher-order diagrams in both the self-energy, Σ, and $I^{(2)}$, which correspond to certain kinds of vertex corrections. In the present simpler description, we neglect these corrections.

A qualitatively important aspect of the derivation is to treat the self-energy terms at the same footing as $I^{(2)}$ so that they are subsumed into a single effective interaction driven by $X^{(2)}_{cvvc}$ explicitly. Also, we consider only the Hartree-Fock contribution to Σ. This is done for consistency, since we perform a resummation of diagrams for $I^{(2)}$ after making the two-time approximations, so that the resulting diagrams are explicitly of first order in the dynamically screened two-particle interaction.

Upon employing the above approximations, the last three terms of Eq. (14) are all captured by a single two-time function denoted below as J, an effective two-particle two-time interaction,

$$\begin{aligned} J[W_{\mathrm{Q}},X^{(2)}](14;1^+4^+) &= iW_{\mathrm{Q}}(14';41')X^{(2)}(1'4;1^+4') \\ &\quad - iW_{\mathrm{Q}}(14;4'1')X^{(2)}(1'4';1^+4^+) \\ &\quad + iW_{\mathrm{Q}}(41';1^+4')X^{(2)}(14';1'4^+) \\ &\quad - iW_{\mathrm{Q}}(4'1';1^+4^+)X^{(2)}(14;1'4'), \end{aligned} \tag{16}$$

which can be considered a function of W and $X^{(2)}$. We define

$$J_{\mathrm{Q}} \equiv J[W_{\mathrm{Q}},X^{(2)}_{\mathrm{Q}}],$$

$$J_2 \equiv J[W_{\mathrm{Q}},\mathfrak{X}^{(2)}_2].$$

Within the two-time approximation, the dynamical maps $\mathcal{M}^{(22;1)}_2$ and $\mathcal{M}^{(22;2)}_2$ can thus be identified from Eq. (16) and can be written as

$$\begin{aligned} \mathcal{M}^{(22;1)}_2\mathfrak{X}^{(2)}_{2cvvc}(14;1^+4^+) &= H_{cc}(1)\mathfrak{X}^{(2)}_{2cvvc}(14;1^+4^+) \\ &\quad + \sigma(11'')J_{\mathrm{Q}cvvc}(11''^+;1^+1'')\mathfrak{X}^{(2)}_{2cvvc} \\ &\quad \times(1''4;1''^+4^+), \end{aligned} \tag{17}$$

$$\begin{aligned} \mathcal{M}^{(22;2)}_2\mathfrak{X}^{(2)}_{2cvvc}(14;1^+4^+) &= -H_{vv}(1^+)\mathfrak{X}^{(2)}_{2cvvc}(14;1^+4^+) \\ &\quad + J_{2cvvc}(11'';1^+1''^+)\sigma(1''4)X^{(2)}_{\mathrm{Q}cvvc} \\ &\quad \times(1''^+4;1''4^+). \end{aligned} \tag{18}$$

In the last two terms, $\sigma(11'') \equiv \sigma(t_1t_1'')$ and we define $\sigma(tt')$ to be $+1$ if $t'>t$ and -1 otherwise. The couplings $\mathcal{M}^{(22;j)}_2$ for $j=3,4$ can be constructed in by ensuring the symmetries discussed in Sec. IVC of I, which we use in Sec. IV below.

By exploiting the structure of $\mathfrak{X}^{(2)}_{2cvvc}(1''4;1''^+4^+)$ on the Keldysh contour and the relationship $iW^<_{\mathrm{Q}}(t't)=iW^>_{\mathrm{Q}}(tt')$, we can verify that the Keldysh matrix for $J(1''4;1''^+4^+)$ has the same matrix structure as $\mathfrak{X}^{(2)}_{2cvvc}(1''4;1''^+4^+)$. Therefore, a matrix with components $\mathcal{J}^{>,<}$, $\hat{\mathcal{J}}^{\pm}$, and $\check{\mathcal{J}}^{\pm}$ can be defined, as discussed in Appendix B. This provides a natural definition for the *retarded* and *advanced* two-particle interaction since it follows that the linear combination,

$$\mathcal{J}^r(tt') \equiv -i\sum_{\alpha,\gamma=\pm}\alpha\gamma J^{\sigma\alpha\sigma'\gamma}(tt'), \tag{19}$$

of the Keldysh components of J vanishes for $t<t'$, while

$$\bar{\mathcal{J}}^a(tt') \equiv i\sum_{\alpha,\gamma=\pm}\sigma\sigma' J^{\sigma\alpha\sigma'\gamma}(tt') \tag{20}$$

vanishes for $t>t'$. These definitions are used in Sec. IV, where we analyze the full equations for $\mathfrak{X}^{(2)}_2$ and discuss their solutions.

Comparing Eq. (16) to the diagrams in Figures I-6(a)–I-6(c), we see that the contributions retained correspond to the top row of Fig. I-6(a). Diagrams in the bottom row of that figure either vanish due to vanishing hole density or contribute with one higher factor of electron density than those in the top row. Diagrams of Fig. I-6(c) will contribute to excitation-induced carrier density effects, mainly EID. We have neglected this as discussed in the previous section and we also comment in Sec. IV on the relevance of this effect to our calculations. Our two-time approximation eliminates diagrams in the top row of Fig. I-6(b). As explained in Appendix B, the two-time approximation for the four-point functions is constructed using the semigroup approximation for the single-particle functions. The latter allows us to subsume the field-dressed quasiparticle lines in these diagrams into J or $X^{(2)}$ in the two-time approximation. In other words, these diagrams are a property of three-time equations only. Diagrams of Figs. I-6(b) and I-6(c) also involve three-particle effects and we turn to our arguments for neglecting them in Sec. III B of this paper.

We conclude with the explicit form of dynamical equations for $\mathfrak{X}^{(1)}_1$ and $\mathfrak{X}^{(2)}_2$ under our approximations for the couplings. In Eq. (12), it is the "+−" Keldysh component that is of interest to us. The derivation in Appendix C, Sec. C 2 shows that for $j=1,2$,

$$\begin{aligned} i\frac{\partial}{\partial t_1}\mathfrak{X}^{(1)+-}_{1;cv}(12) &= \mathcal{S}^{(1;1)}_{1;cv}(12) + [H_{cc}(1)+\Sigma^s_{\mathrm{Q};cc}(1)]\mathfrak{X}^{(1)+-}_{1;cv}(11^+) - iV^s(14';23')\mathfrak{X}^{(1)+-}_{1;cv}(1'3')G^{+-}_{\mathrm{Q}vv}(12) \\ &\quad - iW^{+\sigma-\sigma}_{\mathrm{Q}}(14';41')\cdot[X^{(2)+\sigma-\sigma}_{\mathrm{Q};cvvc}(14';1^+4'^+)\mathfrak{X}^{(1)\sigma\sigma}_{1;cv}(4'^+4'^{++}) - X^{(2)+\sigma-\sigma}_{\mathrm{Q};cvvc}(14';1^+4'^+)\mathfrak{X}^{(1)\sigma\sigma}_{1;cv}(4'^-4')], \end{aligned} \tag{21}$$

$$i\frac{\partial}{\partial t_2}\mathfrak{X}^{(1)+-}_{1;cv}(12) = \mathcal{S}^{(1;1)}_{2;cv}(12) + [H_{vv}(2) + \Sigma^{s}_{\mathrm{Q};vv}(1)]\mathfrak{X}^{(1)+-}_{1;cv}(12) - iG^{+-}_{\mathrm{Q}cc}(12)\mathfrak{X}^{(1)+-}_{1;cv}(1'3')V^{s}(14';23') + iW^{+\sigma-\sigma}_{\mathrm{Q}}(14';41')\cdot[X^{(2)+\sigma-\sigma}_{\mathrm{Q};cvvc}(14;24^{+})\mathfrak{X}^{(1)\sigma\sigma}_{1;cv}(4^{+}4^{++}) - X^{(2)+\sigma-\sigma}_{\mathrm{Q};cvvc}(14;24^{+})\mathfrak{X}^{(1)\sigma\sigma}_{1;cv}(4^{-}4)]. \quad (22)$$

In the above equations, Σ^{s}_{Q} is the singular component of the Hartree-Fock self-energy in which interaction corresponds to the static Coulomb interaction, V^{s}.

The derivation of the couplings for the exciton correlation in the above text yields $\mathcal{M}^{(22;j)}_{2}$ for $j=1,2$ while the equations for $j=3,4$ follow by conjugation. We here write only the former explicitly. In the two-time approximation,

$$\lim_{t_2\to t_1^{+}} i\left(\frac{\partial}{\partial t_1}+\frac{\partial}{\partial t_2}\right)\mathfrak{X}^{(2)}_{2cvvc}(14;24^{+}) = \mathcal{S}^{(2;1)}_{2;cvvc} - \mathcal{S}^{(2;2)}_{2;cvvc}[H_{cc}(1)-H_{vv}(1^{+})]\mathfrak{X}^{(2)}_{2cvvc}(14;1^{+}4^{+}) + \sigma(11'')J_{\mathrm{Q}cvvc}(11''^{+};1^{+}1'')\mathfrak{X}^{(2)}_{2cvvc} \times(1''4;1''^{+}4^{+}) + J_{2cvvc}(11'';1^{+}1''^{+})\sigma(1''4)X^{(2)}_{\mathrm{Q}cvvc}(1''^{+}4;1''4^{+}). \quad (23)$$

It remains to be found the source terms $\mathcal{S}^{(1;j)}_{2;cv}$ and $\mathcal{S}^{(2;j)}_{2;cvvc}$. We now turn to these.

2. Source terms

The source terms, $\mathcal{S}^{(j)}_{p}$, from which $\mathcal{S}^{(j;l)}_{p}$ can be determined as shown in I, originate from the application of the optical pulses to the system and the physical effects captured by them. The interband polarization is driven by the optical fields and these fields are resonant with exciton states; it is thus most conveniently represented in the exciton basis. We represent an exciton state by the ket $|n,\boldsymbol{q}\rangle$, which stands for the exciton state with quantum numbers n and total momentum $\hbar\boldsymbol{q}$. By defining $\alpha_c=m_v/(m_v-m_c)$ and $\alpha_v=m_c/(m_v-m_c)$, momenta for conduction and valence electron in the pair are $\hbar\boldsymbol{k}_c=\hbar(\boldsymbol{k}-\alpha_v\boldsymbol{q})$ and $\hbar\boldsymbol{k}_v=\hbar(\boldsymbol{k}-\alpha_c\boldsymbol{q})$, respectively, such that $\hbar\boldsymbol{k}$ is equal to the reduced mass times relative velocity of the pair. Letting $|\boldsymbol{k}_c,\boldsymbol{k}_v\rangle$ represent the direct product of conduction and valence electron states, we write the eigenfunctions in momentum space as

$$\varphi_{\boldsymbol{q}n}(\boldsymbol{k}) = \langle \boldsymbol{k}-\alpha_v\boldsymbol{q},\boldsymbol{k}-\alpha_c\boldsymbol{q}|n,\boldsymbol{q}\rangle. \quad (24)$$

It is often convenient to express various functions below in the basis $|n,\boldsymbol{q}\rangle$ instead of $|\boldsymbol{k}_c,\boldsymbol{k}_v\rangle$. We write the projection of two point functions, $f_{cv}(\boldsymbol{k}t;\boldsymbol{k}t')$, onto the exciton basis as

$$f_{\boldsymbol{q}n}(tt') = \int \frac{d\boldsymbol{k}}{4\pi^2} f_{cv}(\boldsymbol{k}t;\boldsymbol{k}t')\varphi^{*}_{\boldsymbol{q}n}(\boldsymbol{k}). \quad (25)$$

For deviation of order j in U, such as $\mathfrak{X}^{(1)}_{j;cv}$, we write $\mathfrak{X}^{(1)}_{j;\boldsymbol{q}n}$, etc. Similarly, exploiting the conservation of total momentum of the electron-hole pair, we write the exciton correlation function $X^{(2)}_{cvvc}(14;23)$ in momentum space as $X^{(2)}_{cvvc}(\boldsymbol{k}+\boldsymbol{q},t_1;\boldsymbol{k}'-\boldsymbol{q},t_4|\boldsymbol{k},t_2;\boldsymbol{k}',t_3)$. The transformation to the exciton basis and its inverse are given by

$$X^{(2)}_{\boldsymbol{q}nm}(t_1,t_4;t_2t_3) = \int\frac{d\boldsymbol{k}}{4\pi^2}\int\frac{d\boldsymbol{k}'}{4\pi^2}\varphi^{*}_{\boldsymbol{q}n}(\boldsymbol{k}+\alpha_c\boldsymbol{q})X^{(2)}_{cvvc}(\boldsymbol{k}+\boldsymbol{q},t_1;\boldsymbol{k}'-\boldsymbol{q},t_4|\boldsymbol{k},t_2;\boldsymbol{k}',t_3)\varphi_{\boldsymbol{q}m}(\boldsymbol{k}'+\alpha_v\boldsymbol{q}), \quad (26)$$

$$X^{(2)}_{cvvc}(\boldsymbol{k}+\boldsymbol{q},t_1;\boldsymbol{k}'-\boldsymbol{q},t_4|\boldsymbol{k},t_2;\boldsymbol{k}',t_3) = \sum_{nm}\varphi_{\boldsymbol{q}n}(\boldsymbol{k}+\alpha_c\boldsymbol{q})X^{(2)}_{\boldsymbol{q}nm} \times(t_1,t_4;t_2t_3)\varphi^{*}_{\boldsymbol{q}m}(\boldsymbol{k}'+\alpha_v\boldsymbol{q}), \quad (27)$$

which also applies to $\mathcal{S}^{(j;l)}_{n;cvvc}$.

We turn now to optical excitation. For states with the parity opposite to the states at the top of the valence band, the source driving first-order interband polarization can be characterized by its projection onto the exciton states[12]

$$U_{\boldsymbol{q}n}(t) = \delta_{\boldsymbol{q}}\int\frac{d\boldsymbol{k}}{4\pi^2}U_{cv}(\boldsymbol{k}t;\boldsymbol{k}t^{+})\varphi^{*}_{\boldsymbol{q}n}(\boldsymbol{k})$$

$$U_{cv}(\boldsymbol{k}t;\boldsymbol{k}t^{+}) = -\frac{e}{\hbar}\mathcal{E}(t)e^{-i\omega t}\boldsymbol{\xi}_{cv}(\boldsymbol{k}). \quad (28)$$

Here, $\mathcal{E}(t)$ is the envelope function. Parity-forbidden states are excited by two-photon absorption[15]

$$U_{cv}(\boldsymbol{k}t;\boldsymbol{k}t^{+}) = -\frac{e}{\hbar}\mathcal{E}'^{i}(t)\mathcal{E}'^{j}(t)e^{-i2\omega' t}\eta^{ij}_{cv},$$

where η^{ij}_{cv} are the Cartesian tensor components of the two-photon transition. The center frequencies ω and $2\omega'$ are assumed to overlap with the excitation energy of exciton states with respect to the ground state. Only excitons with a zero total momentum, $\boldsymbol{q}=0$, are generated owing to the neglect of the photon momentum. The source terms $\mathcal{S}^{(1;j)}_{1}$ that drive first-order deviation of the Green's function (21) and (22) are essentially these effective energies

$$\mathcal{S}^{(1;1)}_{1;cv}(12) = U_{cv}(1)G_{vv}(12), \quad (29)$$

$$\mathcal{S}^{(1;2)}_{1;cv}(12) = G_{cc}(12)U_{cv}(2). \quad (30)$$

The two-particle source terms are considerably more complicated and the approach presented in I was in large measure developed to allow for their formulation. Again, we rely on I and sketch the derivation of the expressions for these terms within our approximations. One of the advantage of the approach of I is the establishment of a diagrammatic approach that simplifies the identification and use of such approximations and depicts the underlying many-body phys-

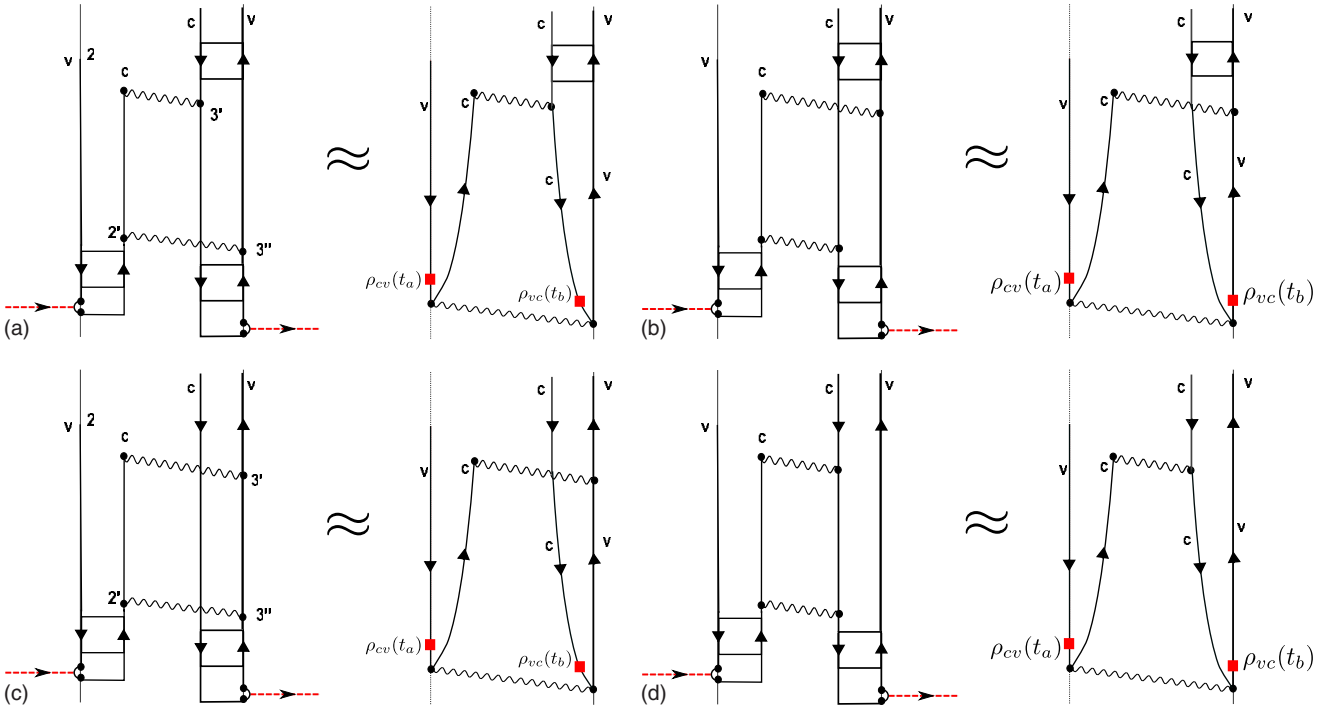

FIG. 1. (Color online) Source diagrams for $\mathcal{S}_2^{(2)}$: top row corresponds to ΔI_1 terms and the bottom to $\mathfrak{X}_1^{(2)}$ terms. For each diagram, switch c and v lines on the positive branch for the diagrams to complete the set. Note that the interaction vertex and the interband polarization are placed at equal times and the separation is shown only for clarity. The approximation is discussed in the text.

ics. We follow this approach below, where we must refer the reader to I for many of the equations and the diagrammatic rules; the final result, in the exciton basis, is given by Eqs. (34) and (35). The result shows that the interband coherence drives the source for the correlation function for excitons. This makes explicit the transfer of interband coherence to the exchange-correlation part of the Raman coherence.

The source terms $\mathcal{S}_{2;cvvc}^{(2;j)}(tt')$ are related to the optical field only via the effect of the field on the single-particle propagators. More precisely, the source term of second order in the field arises from the products of the first-order correlations [see I-(102)]. We are interested in the "lesser" component, "+−+−." Leaving the details elsewhere[20] and in the notation of I, we have

$$\mathcal{S}_{2;cvvc}^{(2;1)}(t_1,t_2) = \mathfrak{X}_{1;cv}^{(1)}(2'2) \times \left\{ \Delta I_{1;cvcc}(1'2'';2'1'') P_{\mathrm{Q}cvvc}(1''4;2''3) + \sum_{\zeta} I_{\mathrm{Q};c\zeta c\zeta}(1'2'';2'1'') \mathfrak{X}_{1;\zeta v\zeta c}^{(2)}(1''4;2''3) \right\}, \tag{31}$$

$$\mathcal{S}_{2;cvvc}^{(2;2)}(t_1,t_2) = \mathfrak{X}_{1;cv}^{(1)}(11') \times \left\{ \Delta I_{1;vvvc}(1'2'';2'1'') P_{\mathrm{Q}cvvc}(1''4;2''3) + \sum_{\zeta} I_{\mathrm{Q};v\zeta v\zeta}(1'2'';2'1'') \mathfrak{X}_{1;\zeta v\zeta c}^{(2)}(1''4;2''3) \right\}. \tag{32}$$

We consider diagrams of the lowest order in the dynamical interaction. In the four left sides of the panels in Fig. 1, we show the four diagrams that contribute to $\mathcal{S}_{2;cvvc}^{(2;1)}$; the diagrams for $\mathcal{S}_{2;cvvc}^{(2;2)}$ are constructed by switching G_{cc} and G_{vv} lines on the positive contour. In each of the four panels, the left-hand side shows the exact diagram in which the arrows represent $U_{cv}(\boldsymbol{kt};\boldsymbol{kt}^+)$ generating pairs. The pair is in general correlated as represented by the box that the two lines following the pulse enter. In these diagrams, both the "bra" and "ket" sides of the diagram are linked to a field line since there is no population of excitons in the equilibrium state. This immediately tells us that coherence in the two-particle states is necessarily of the second order in the field in this scenario. In contrast, in a finite pre-existing population of excitons, diagrams where the two field lines lie on the same contour would also survive. They would represent the response of the exciton population to the second order in the driving field.

Finally, we see that in accordance with the rule that only fully connected diagrams are allowed,[12] the two correlated pairs interact with each other. At this lowest order, there are two interaction lines because all diagrams with a single such line are accounted for in the definition of $W_{\mathrm{Q}}^{\lessgtr}$ (see also Ref. 12). Since they are on the opposite sides of the Keldysh contour, the interaction must be $W_{\mathrm{Q}}^{\lessgtr} = W_{\mathrm{Q}}^{r} \chi_{\mathrm{Q}}^{\lessgtr} W_{\mathrm{Q}}^{a}$, where χ_{Q} is the longitudinal susceptibility and therefore is a purely dynamic response. This is in agreement with the discussion following Eq. (7) where the buildup of correlations is attributed to mainly to the response of the medium. The source term will vanish identically in the zero quasiparticle density or, more generally, in the absence of dynamical and exchange effects. This is so because, as discussed earlier, the

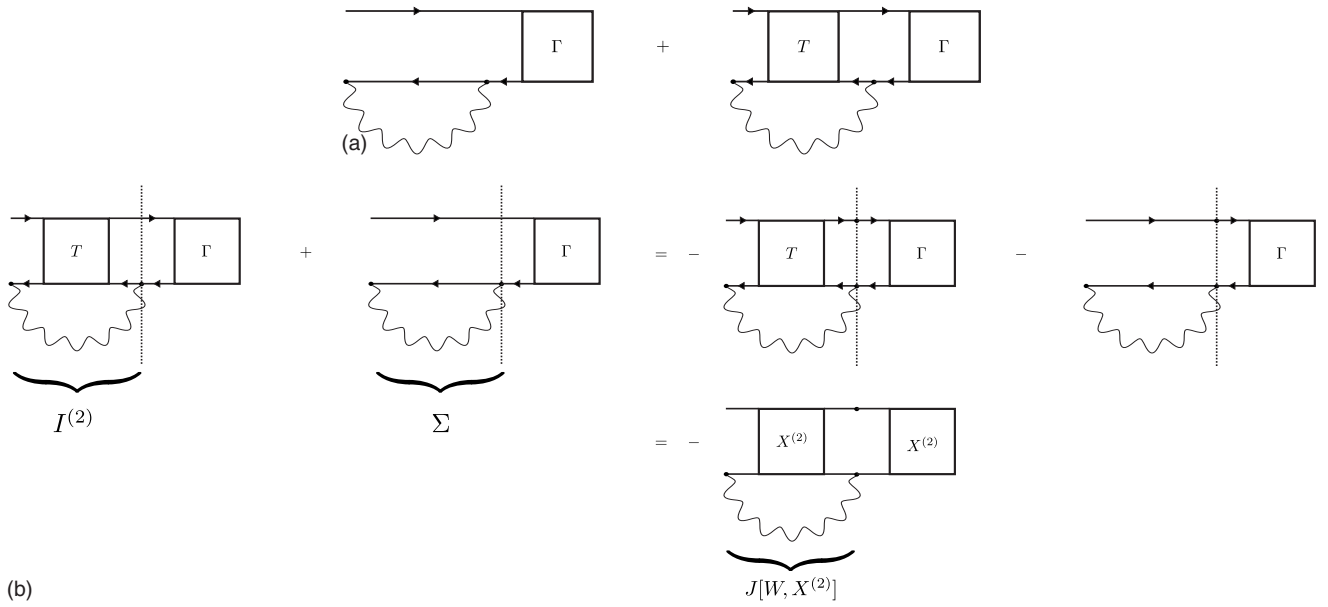

FIG. 2. (a) Diagrams used in deriving Eq. (16). Symbols are defined in I. (b) Semigroup approximation applied to the above diagrams.

"amplitudes" $G_{cv}(11^+)$ in this case fully describe the system with a perfectly coherent evolution.

In these diagrams, the pulse connected to a two-particle correlation yields the functions $\mathfrak{X}^{(1)}_{1;cv}(2'2)$ on the positive branch and $\mathfrak{X}^{(1)}_{1;vc}(3''3')$ on the negative branch by definition. Therefore, a full solution of the Dyson equation varied to first order in the field can be inserted to compute the diagrams. However, it is useful to analyze these diagrams using the approximate semigroup approximation, which in this case is also equivalent to using the generalized Kadanoff-Baym ansatz. In this approximation, only the advanced Green's function contributes since the time ordering, $t_2 > t_{2'}$, is fixed by the zero hole density of the equilibrium state and thus

$$\mathfrak{X}^{(1)}_{1;cv}(2'2) = \rho(2')G^a_{\mathcal{Q}vv}(2'2), \tag{33}$$

where ρ is defined in Eq. (11). In the four right-hand panels of Fig. 1, we show the result of applying this approximation to the diagrams in the left-hand panels. We have represented ρ_{cv} and ρ_{vc} in the right-hand panels by squares. Note that there is no interaction placed between the $G_{\mathcal{Q}cc}$ and $G_{\mathcal{Q}vv}$ to make another correlated pair on the right-hand side diagrams.[21]

The diagrams in the right-hand panels connect the interband coherence with the memory of the system and show more clearly how the coherence in $\mathfrak{X}^{(2)}_{2;cvvc}$ arises. To see this in detail, we begin by noting that by definition, $G^<_{cv}$ can be written as

$$G^<_{cv}(tt') = i\,\mathrm{Tr}[a_v^\dagger \mathcal{U}(t',t)a_c\mathcal{U}(t,t_0)\varrho_{\mathcal{Q}}\mathcal{U}(t_0,t)] = i\,\mathrm{Tr}[a_v^\dagger \mathcal{U}(t',t) \times \{a_c\varrho(t)\}],$$

where $\varrho_{\mathcal{Q}}$ is the many-body statistical operator describing the equilibrium background state. The $\mathcal{U}$ are exact evolution operators and we use the cyclic property of the trace to obtain the second line. The term $a_c\varrho(t)$ represents the removal of a conduction electron from the state as it evolves from the initial time t_0 to the time t. It is clear from Fig. 2(a) that $t' > t$ and therefore the modified state evolves from t to t' and at the latter time a valence electron is added to it. The sufficient condition for the trace to be nonzero is that coherence between the conduction and the valence band exist in $\varrho(t)$. Beyond time t, the state evolves with an extra valence hole or a missing valence electron. This is described precisely by the function $G_{\mathcal{Q}vv}(t't)$ as the interaction with the field has occurred before time t. Now, the phase-breaking time of the quasiparticle propagator $G_{\mathcal{Q}vv}$ is given by the on-shell inverse imaginary self-energy, $\Im\Sigma_{\mathcal{Q}vv}$, and it can be much longer than the decoherence time of the interband polarization. Therefore, the amplitude $\mathfrak{X}^{(1)}_{1;cv}(2'2)$ exists for t_2 beyond $t_{2'}+t_{dec}$, where t_{dec} is the time span over which ρ_{cv} vanishes. Since the two-particle correlation forms from the interaction of single-particle correlations, it becomes clear that coherence in the two-particle function can form within the phase-breaking time of the quasiparticle once an interband polarization has formed. This is essentially the content of the propagators linking the two interaction lines in the right-hand panels of Fig. 2(a). Once a summation over momentum of the propagators is performed, the inhomogeneous broadening will further restrict the temporal spread of the coherence. The interaction lines themselves control the maximum delay between the interband polarizations that is allowed such that coherence can be transferred to $\mathfrak{X}^{(2)}_{2;cvvc}$. Therefore, the time delay between the two optical pulses, which is an experimental parameter, is equal to τ in $W^<_{\mathcal{Q}}(\tau)$ and its variation leads to a probe of that function.

As mentioned earlier, the 4×4 matrix (in contour indices) corresponding to $X^{(2)}$ takes a special form with six different components. We use these components, and Eqs. (25) and (26), to write source term $\mathcal{S}^{(2;1)}_{2;cvvc}$ in the exciton bases. The subscript used for indicating the order in U in $\mathcal{S}^{(2)}_2$ is always 2 when appearing explicitly. For brevity, we will omit this subscript.[22] Thus, we will write $\mathcal{S}^{(2;1)}_{2;cvvc}$ as $\mathcal{S}^{(2;1)}_{cvvc}$ and its projection onto the exciton states as

$$\mathcal{S}^{(2;1)}_{\boldsymbol{q}nm}(t,t') = e^{-i(\omega_{\boldsymbol{q}n}t-\omega_m t')}\int_0^\infty d\tau_a\int_0^\infty d\tau_b\int_0^\infty d\tau' \mathcal{P}^{>}_{\mathrm{Q};\boldsymbol{q}mm}(-\tau')\mathcal{R}^{c}_{\boldsymbol{q}nm;n'm'}(\tau_a,\tau_b,\tau')\rho_{\boldsymbol{q}n'}(t-\tau_a)\rho^{*}_{\boldsymbol{q}m'}(t'-\tau_b-\tau'), \tag{34}$$

$$\mathcal{S}^{(2;2)}_{\boldsymbol{q}nm}(t,t') = \mathcal{S}^{(2;1)}_{2;\boldsymbol{q}nm}(t,t') = e^{-i(\omega_n t-\omega_m t')}\int_0^\infty d\tau_a\int_0^\infty d\tau_b\int_0^\infty d\tau' \mathcal{P}^{>}_{\mathrm{Q};\boldsymbol{q}mm}(-\tau')\mathcal{R}^{v}_{\boldsymbol{q}nm;n'm'}(\tau_a,\tau_b,\tau')\rho_{\boldsymbol{q}n'}(t-\tau_a)\rho^{*}_{\boldsymbol{q}m'}(t'-\tau_b-\tau'), \tag{35}$$

where the "response function" is

$$\mathcal{R}^{\eta}_{\boldsymbol{q}nm;n'm'}(\tau_a,\tau_b,\tau') = \int d\boldsymbol{q}' W^{<}_{\mathrm{Q}}(\boldsymbol{q}-\boldsymbol{q}',\tau')W^{>}_{\mathrm{Q}}(\boldsymbol{q}',\tau+\tau'+\tau_b-\tau_a)f^{\eta\eta}_{nn'}(\boldsymbol{q}-\boldsymbol{q}',\boldsymbol{q}'|\tau_a)\sum_{\zeta\zeta'}(1-2\delta_{\zeta\zeta'})f^{\zeta\zeta'*}_{mm'}(\boldsymbol{q}-\boldsymbol{q}',\boldsymbol{q}'|\tau_b). \tag{36}$$

The correlation functions of the bath are represented by $W^{\lessgtr}_{\mathrm{Q}}$ and can be interpreted as absorption and emission of the electron gas excitations, where a total momentum of $\boldsymbol{q}$ is gained by the pair via the two interactions. The factor $1-2\delta_{\zeta\zeta'}$ accounts for the change in sign of the interaction when conduction electron and a valence hole are involved. The functions $f_{nn'}(\cdot,\cdot,\cdot)$ are defined as

$$f^{\zeta\zeta'}_{nn'}(\boldsymbol{q}-\boldsymbol{q}',\boldsymbol{q}',\tau) = \int \frac{d\boldsymbol{k}}{4\pi^2}\varphi^{*}_{\boldsymbol{q}n}[\boldsymbol{k}+\alpha_\zeta(\boldsymbol{q}-\boldsymbol{q}')]\varphi_{\boldsymbol{0}n'}(\boldsymbol{k}-\alpha_{\zeta'}\boldsymbol{q}')G_{\mathrm{Q}cc}(\boldsymbol{k}-\alpha_v\boldsymbol{q},\tau)G_{\mathrm{Q}vv}(\boldsymbol{k}-\alpha_c\boldsymbol{q}',-\tau), \tag{37}$$

where the propagators in Eq. (37) represent the evolution of the pair for a time delay, τ, between the two scattering events.

In the two-time plane (t,t'), the direction of macroscopic evolution of the system occurs along lines of constant $\tau=t-t'$. Along this line, the propagation is driven by the difference of the two source terms, which vanishes for $\boldsymbol{q}=\boldsymbol{q}'=0$. Thus, any nonzero momentum exchange necessarily occurs in the driving terms. From Eq. (37), we also see that the distribution of the state in momentum space strongly "filters" the memory effects of the quasiparticles. States that are tightly bound would generally produce less smearing of the interband polarization than those that are loosely bound and therefore their driving terms will more closely follow the direct beating of the interband polarizations. Higher-energy states will restrict the total number of excitations of the electron gas contributing to this source to fewer numbers and will therefore have longer-lasting driving term but it will have a lower amplitude. Furthermore, we see the competing effects of density, whereby the larger density yields a larger source term, but lowers its duration at the same time. These observations are confirmed in the numerical calculations presented below.

When we restrict the above expressions to the isotropic model, the angular integrations over $\boldsymbol{q}'$ suppress transitions among states of different parity. Thus, the elements $\mathcal{R}_{\boldsymbol{q}nm;n'm'}$ are nonzero only if the difference in parity between n and n' is the same as that between m and m'. In particular, this implies that if the directions for fields that excite the two states $|n,\boldsymbol{q}\rangle$ and $|m,\boldsymbol{q}\rangle$ are $\hat{\boldsymbol{k}}_n$ and $\hat{\boldsymbol{k}}_m$, then the coherence driven by $\mathcal{S}_{nm}$ and $\mathcal{S}_{mn}$ will radiate in directions $\hat{\boldsymbol{k}}_n-\hat{\boldsymbol{k}}_m+\hat{\boldsymbol{k}}_3$ and $\hat{\boldsymbol{k}}_m-\hat{\boldsymbol{k}}_n+\hat{\boldsymbol{k}}_3$, respectively; the vector $\hat{\boldsymbol{k}}_3$ is the direction of the third field amplitude that generates the signal. This clean separation is an advantage of two-dimensional Fourier spectroscopy.

Equations (34) and (35) express the source terms in exciton basis. Their transformation back to the single-particle basis is effected by Eq. (27). Substitution of Eqs. (28) and (34) (after transformation to single-particle basis) into Eqs. (21) and (22), respectively, completes the equations of motion within the set of approximations adopted here. In the next section, we discuss the regime of validity of these approximations and the physics that is retained or neglected. Section IV below is devoted to the solution of these equations, where they are put into a simplified form suitable for both the analysis in that section and the numerical calculations that follow.

B. Discussion of approximations

The mathematical details of the reduction from three-time to two-time equations are elaborated in Appendix B. It is the semigroup approximation for the fully interacting Green's functions mentioned earlier. We applied it to diagrams shown in Fig. 2(a), arising in expressions such as Eqs. (12) and (13) and obtained the results [Eqs. (21)–(23)] of Sec. III. In this section, we discuss (a) the diagrams that are beyond those in Fig. 2(a) and (b) the diagrams that are in Fig. 2(a) but have been neglected by the semigroup approximation.

We first return to the mathematical consequences of neglecting holelike excitations in the conduction band and particlelike in the valence band. When applying the semigroup approximation to diagrams such as those in Fig. 2(a), the diagram is cut in two pieces at the vertex where the interaction line joins the particle line as shown in Fig. 2(b). The approximation is in insisting on the temporal direction of the Green's function lines at the top of the diagram (where there is no interaction placed). Thus, in these diagrams, the line at the top corresponds to valence electron and is assumed to flow backward at the point where it is cut. This introduces a minus sign, as shown on the right-hand side of the diagrammatic equation in that figure.

We neglected the vertex corrections to the self-energy in the diagrams of Fig. 2(a). They can be included within the two-time approximation. The leading vertex corrections in the self-energy are shown in Fig. 3. These diagrams represent the process where a virtual electron-hole pair in the conduction-band forms at the time, t'. The electron in this pair is exchanged with the electron bound to the valence hole

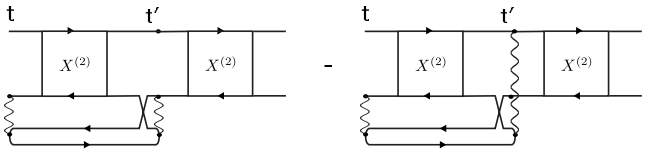

FIG. 3. Leading-order vertex corrections to self-energy. These diagrams exchange an electron in the bound pair with one in a virtual excitation in the background gas. Symbols are defined in I.

in $X^{(2)}$ while the electron from $X^{(2)}$ annihilates the conduction hole at time t. Applying the diagram rules in I, the effect of these diagrams is to add the exchange corrections to the screened interaction W in Eq. (16). Naturally, the contribution of the additional term exists only at high densities where the exchange process can be significant. In any case, at low frequencies, it is dominated by the plasma excitations contained in W, which contribute a large response. In the calculations below, we neglect this particular contribution of exchange process but remark that the subsequent analysis remains valid even if it is included.

The leading diagrams that are part of Fig. 2(a) but are neglected in the two-time approximation are of the form

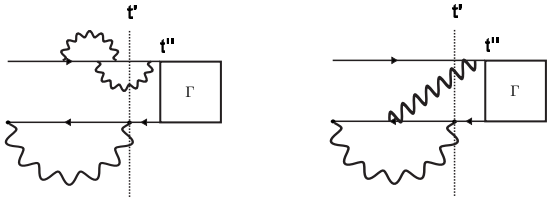

These diagrams are proportional to one higher power of density of the electron gas than the ones retained. This is so because they involve a finite-time interval over which a virtual electron-hole pair must propagate and interact with the two correlated electrons. Such four-particle complexes may become important in high-density plasmas, but not at small densities in the present parameter regime. Furthermore, including them will not introduce new poles in the two-particle spectrum; they will only adjust the spectrum quantitatively in the complex domain. It should be noted that including these diagrams does not necessarily break the two-time structure. They can be decomposed further into a product of two-time correlations, but doing so transforms a single expression for three-time effective interaction to a sum over infinite two-time effective interactions in the equations of motion. Nonetheless, when a finite number of these can be identified as capturing the desired physics, the two-time approximation becomes useful a computational tool.

We emphasize the difference between our approach and that of Bornath *et al.*,[23] who also employed the semigroup properties up to second order in their perturbation expansion and identified a two-particle self-energy by regrouping the expressions. Their expressions for the two-particle self-energy, which are analogous to J in Eq. (16), depend only on the single-particle propagators. Their procedure must be infinitely repeated to identify the contribution of the two-particle propagator. The expressions obtained are the kinds that are useful in discussing high-density plasmas where collisions among electrons rather than the self-consistent propagation of a bound pair dominate the physics. On the other hand, in the ansatz (16), the contribution of a pair of conduction and valence electrons to the self-energy is assumed to be dominated by the two-particle properties of the pair rather than single-particle properties. This is done to include self-consistently the back-action of an exciton on itself via its interaction with the electron gas. Such a back-action makes an important qualitative contribution to the decoherence phenomenon as discussed below. Besides the contribution of the exciton, there are also contributions of two-particle functions where both particles belong to the same band. We neglect these, since their effect does not change the dynamics qualitatively.

IV. DYNAMICS

We now return to Eqs. (21)–(23) and substitute into them the source expressions [Eqs. (29), (30), (34), and (35)] derived above. These are the dynamical equations we wish to solve.

We will first obtain a physically intuitive form for Eq. (23). In Appendix C, Sec. C 1, we define a set of six functions for the two-time approximation to the components of Keldysh matrix of four-point functions. We show that within the two-time limit, the function $\mathcal{P}^{<}(t,t')$ from this set corresponds to $X^{(2)+-+-}_{cvvc}(14;1^+4^+)$ and thus also to $\mathfrak{X}^{(2)+-+-}_{cvvc}(14;1^+4^+)$. The derivation in Appendix C results in the following equation:

$$
\begin{aligned}
i\frac{\partial}{\partial t}\mathcal{P}^{<}(tt') - \mathcal{H}_{eff}\mathcal{P}^{<}(tt') &= \mathfrak{X}^{<}_{vv}(t't) - \mathfrak{X}^{>}_{cc}(tt') \\
&- \int_{t_{min}}^{t_{max}} \mathcal{J}^{r}_{\mathrm{Q}}(tt'')\mathcal{P}^{<}(t''t') + \mathcal{J}^{<}_{\mathrm{Q}}(tt'')\mathcal{P}^{a}(t''t') \\
&- i\int_{-\infty}^{t_{min}} \mathcal{J}^{<}_{\mathrm{Q}}(tt'')\mathcal{P}^{>}(t''t') + \mathcal{J}^{>}_{\mathrm{Q}}(tt'')\mathcal{P}^{<}(t''t')dt'' \\
&+ \int_{t_{min}}^{t_{max}} \mathcal{J}^{r}(tt'')\mathcal{P}^{<}_{\mathrm{Q}}(t''t') + \mathcal{J}^{<}(tt'')\mathcal{P}^{a}_{\mathrm{Q}}(t''t') \\
&+ i\int_{-\infty}^{t_{min}} \mathcal{J}^{<}(tt'')\mathcal{P}^{>}_{\mathrm{Q}}(t''t') + \mathcal{J}^{>}(tt'')\mathcal{P}^{<}_{\mathrm{Q}}(t''t')dt'' \\
&+ i\int_{-\infty}^{t_{min}} \hat{\mathcal{J}}^{-}_{\mathrm{Q}}(tt'')\check{\mathcal{P}}^{+}(t''t') + \hat{\mathcal{J}}^{+}_{\mathrm{Q}}(tt'')\check{\mathcal{P}}^{-}(t''t')dt'' \qquad (38)
\end{aligned}
$$

$$
- i\int_{-\infty}^{t_{min}} \hat{\mathcal{J}}^{-}(tt'')\check{\mathcal{P}}^{+}_{\mathrm{Q}}(t''t') + \hat{\mathcal{J}}^{+}(tt'')\check{\mathcal{P}}^{-}_{\mathrm{Q}}(t''t')dt''. \qquad (39)
$$

Here, $\mathcal{H}_{eff}$ is an effective Hamiltonian that defines the nominal exciton energies calculated self-consistently within a model for the equilibrium electron gas (see Sec. V). The row vector $\mathcal{J}(tt')$ has been discussed in Sec. III. The precise form of all its components, $\mathcal{J}^{\lessgtr}$, $\hat{\mathcal{J}}^{\pm}$, $\check{\mathcal{J}}^{\pm}$, is derived in Appendix C, Sec. C 3. The equation applies to both above and below the time diagonal $t=t'$, where $t_{min}=\min(t,t')$ and $t_{max}=\max(t,t')$. The equation for derivative with respect to the second argument, $\partial\mathcal{P}^{<}(tt')/\partial t'$, is obtained by using the relation $\mathcal{P}^{<}(t,t')=\mathcal{P}^{<\dagger}(t',t)$. We will explicitly treat only the

region $t>t'$ since the other half of the time plane is related by Hermitian conjugation and time reversal.

Equation (38) is not restricted to vanishing density of holes and excitons in the equilibrium state, but we take this limit by setting $\mathcal{P}_{\mathrm{Q}}^{<}$ and $\mathcal{J}_{\mathrm{Q}}^{<}$ equal to zero. We also omit the first term on the right-hand side, which involves single-particle Green's functions, and the last term which involves $\hat{\mathcal{P}}$ functions, etc. The former will cancel out when the equations are subtracted to obtain dynamics parallel to the time diagonal in the two-time plane. The latter is one order of density higher than others and so is small in the regime where at least two exciton states are stable. We drop all those terms containing $\mathcal{J}_{\mathrm{Q}}^{<}$ and $\mathcal{P}_{\mathrm{Q}}^{<}$ because they are proportional to the equilibrium density of excitons, which is zero. Note that in keeping with the approximation to neglect the terms involving $\check{\mathcal{J}}_{\mathrm{Q}}$, $\hat{\mathcal{J}}_{\mathrm{Q}}$, we have dropped them from the retarded functions as well and thus

$$\mathcal{J}_{\mathrm{Q}}^{r}(tt') \approx -i\mathcal{J}_{\mathrm{Q}}^{>}(tt')\theta(t-t'),$$

$$\mathcal{P}_{\mathrm{Q}}^{r}(tt') \approx -i\mathcal{P}_{\mathrm{Q}}^{>}(tt')\theta(t-t').$$

Substitution of these expressions (and their conjugates for the advanced functions) into Eq. (38) yields

$$i\frac{\partial}{\partial t}\mathcal{P}^{<}(tt') - \mathcal{H}_{eff}\mathcal{P}^{<}(tt') = \mathcal{S}^{(2;1)}(tt') + i\int_{-\infty}^{t'}\mathcal{J}^{<}(tt'')\mathcal{P}_{\mathrm{Q}}^{>}(t''t')dt'' - i\int_{-\infty}^{t}\mathcal{J}_{\mathrm{Q}}^{>}(tt'')\mathcal{P}^{<}(t''t')dt'', \tag{40}$$

$$-i\frac{\partial}{\partial t'}\mathcal{P}^{<}(tt') - \mathcal{P}^{<}(tt')\mathcal{H}_{eff} = \mathcal{S}^{(2;2)}(tt') - i\int_{-\infty}^{t}\mathcal{P}_{\mathrm{Q}}^{>}(tt'')\mathcal{J}^{<}(t''t')dt'' + i\int_{-\infty}^{t'}\mathcal{J}^{<}(tt'')\mathcal{P}_{\mathrm{Q}}^{>}(t''t')dt''. \tag{41}$$

When the expressions for $\mathcal{J}^{\lessgtr}$, given in Appendix C, Sec. C 3, are substituted in Eqs. (40) and (41), we obtain

$$\left(\frac{\partial}{\partial t_1}+\frac{\partial}{\partial t_2}\right)\mathcal{P}_{\boldsymbol{q}nm}^{<}(t_1,t_2) + i[\mathcal{H}_{eff},\mathcal{P}_{\boldsymbol{q}nm}^{<}(t_1,t_2)] = \mathcal{S}_{\boldsymbol{q}nm}(t_1,t_2) + \int_{-\infty}^{t_2}dt''\Bigg[-\mathcal{P}_{\boldsymbol{q}nm'}^{<}(t_1t'')\mathcal{B}_{m'm}(\boldsymbol{q}|t''-t_2) + \int\frac{d\boldsymbol{q}'}{4\pi^2}\mathcal{C}_{nm;n'm'}(\boldsymbol{q},\boldsymbol{q}'|t_1-t'',t''-t_2)\mathcal{P}_{\boldsymbol{q}'n'm'}^{<}(t_1t'')\Bigg]\int_{-\infty}^{t_1}dt''\Bigg[-\mathcal{B}_{nn'}(\boldsymbol{q}|t_1-t'')\mathcal{P}_{\boldsymbol{q}n'm}^{<}(t''t_2) + \int\frac{d\boldsymbol{q}'}{4\pi^2}\mathcal{C}_{nm;n'm'}(\boldsymbol{q},\boldsymbol{q}'|t''-t_2,t_1-t'')\mathcal{P}_{\boldsymbol{q}'n'm'}^{<}(t''t_2)\Bigg]. \tag{42}$$

The source term follows from the difference of Eqs. (34) and (35) and the addition of the conjugate terms for the rest of the two arguments

$$\mathcal{S}_{\boldsymbol{q}nm}(t,t') = \mathcal{S}_{\boldsymbol{q}nm}^{(2;1)}(t,t') - \mathcal{S}_{\boldsymbol{q}nm}^{(2;2)}(t,t') + \mathcal{S}_{\boldsymbol{q}mn}^{(2;1)*}(t',t) - \mathcal{S}_{\boldsymbol{q}mn}^{(2;2)*}(t',t).$$

We have written the expression for the interaction as a superoperator, $\mathcal{C}$, that maps matrices to matrices

$$\mathcal{C}_{nm;n'm'}(\boldsymbol{q},\boldsymbol{q}'|\tau,\tau') = iW_{\mathrm{Q}}^{<}(\boldsymbol{q}-\boldsymbol{q}'|\tau)A_{nn'}(\boldsymbol{q},\boldsymbol{q}')A_{m'm}(\boldsymbol{q}',\boldsymbol{q})\mathcal{P}_{\mathrm{Q};\boldsymbol{q}mm}^{>}(\tau') \tag{43}$$

and as a matrix $\mathcal{B}$ related to $\mathcal{C}$ via

$$\mathcal{B}_{mm'}(\boldsymbol{q}|\tau) = \sum_j\int d\boldsymbol{q}'\mathcal{C}_{jj;m'm}(\boldsymbol{q}',\boldsymbol{q}|-\tau,\tau). \tag{44}$$

The matrix A is given by

$$A_{nm}(\boldsymbol{q},\boldsymbol{q}') \equiv O_{nm}(\alpha_c\boldsymbol{q},\alpha_c\boldsymbol{q}') - O_{nm}(\alpha_v\boldsymbol{q},\alpha_v\boldsymbol{q}'), \tag{45}$$

with

$$O_{nm}(\boldsymbol{q},\boldsymbol{q}') = \langle n,\boldsymbol{q}|e^{-i(\boldsymbol{q}-\boldsymbol{q}')\cdot\hat{\mathbf{r}}}|m,\boldsymbol{q}'\rangle = \int\frac{d\boldsymbol{k}}{4\pi^2}\varphi_{\boldsymbol{q},n}^{*}(\boldsymbol{k}+\boldsymbol{q})\varphi_{\boldsymbol{q}'m}(\boldsymbol{k}+\boldsymbol{q}').$$

The leading contribution to A (for small $\boldsymbol{q}-\boldsymbol{q}'$) is the dipole or the quadrupole matrix elements of the exciton.

Thus the physical process that determines A (or $\mathcal{C}$) is the scattering of the surrounding gas by the electron-hole pair. In a calculation, the transfer of momentum to the pair as a result of this scattering appears through virtual or real transitions among the internal states of the exciton. The transfer of momentum via electron or hole corresponds to $O_{nm}(\alpha_c\boldsymbol{q},\alpha_c\boldsymbol{q}')$ or $O_{nm}(\alpha_v\boldsymbol{q},\alpha_v\boldsymbol{q}')$, respectively. A quasiparticle interacting with the exciton sees a neutral particle, unless the scattering process is sensitive to the composite nature of the exciton. As shown in Appendix C, Sec. C 3, this matrix arises naturally in the derivation where contributions from the composite functions are also retained.

We note that when Eq. (44) is substituted into Eq. (42), a conservation law follows

$$\frac{\partial}{\partial t}\sum_n\int d\boldsymbol{q}\mathcal{P}_{\boldsymbol{q}nn}^{<}(t,t) = \sum_n\int d\boldsymbol{q}\mathcal{S}_{\boldsymbol{q}nn}(tt).$$

Physically, this is a consequence of ascribing all the interband transitions to the optical excitation so that the Coulomb interaction composing the dynamical map cannot create or annihilate excitons. Thus, the set of approximations employed in deriving this map respects this property of the Hamiltonian exactly.

The single-particle equation, written for the $\rho_{\boldsymbol{q}n}(t)$ defined in Eq. (25), obeys an equation that involves only the $\mathcal{B}$ matrix (see Appendix C, Sec.C 2)

$$\left(\frac{d}{dt}+i\omega_{\boldsymbol{q}n}\right)\rho_{\boldsymbol{q}n}(t)=U_{\boldsymbol{q}n}(t)+\int_0^\infty d\tau\mathcal{B}_{nm}(\boldsymbol{q}|\tau)\rho_{\boldsymbol{q}m}(t-\tau). \tag{46}$$

Equations (42) and (46) are the main results of this paper. The rest of this section is devoted to their analysis and determining the main properties of their solutions.

A defining property of the map $\mathcal{C}$, which is expected to hold at any level of approximation, can be taken to be its relationship (44) to $\mathcal{B}$ and the single particle Eq. (46). This is so because all those diagrams in the equation where the interaction acts only on one side of the function $\mathcal{P}^<$ can be closed on the other side using a $\mathfrak{X}_{1;cv}$ line to form a contribution to the equation for interband polarization. Thus, these diagrams generate self-coupling in the equation for $\mathfrak{X}_{1;cv}$. Diagrams that contribute to $\mathcal{C}$ contain at least two optical excitations already and therefore can only contribute to sources at third or higher order, or they can appear as cross coupling in the full set of second-order equations.

We now consider the generation of excitons with a finite total momentum, $\boldsymbol{q}$. While Eq. (28) strictly restricts the interband polarization to $\boldsymbol{q}=0$, the interactions of these polarizations via pair excitations can result in a transfer of momentum from the electron gas to the exciton. While the momentum transferred will have an average value of zero, $\langle\boldsymbol{q}^2\rangle$ will in general be finite so that $\mathcal{S}^{(2)}_{\boldsymbol{q}nm}(tt')$ will have a finite spread in momentum space. As the Kubo-Martin-Schwinger (KMS) relations[24–26] imply that $W^{\lessgtr}(q,\omega)\propto V(q)\Im\varepsilon_{\mathrm{Q}}^{-1}(q,\omega)$, this spread decays at least as $1/q$. It is further suppressed by the form factors, which at large $\boldsymbol{q}$ decay as q^{-3} for s states and q^{-4} for p states, as implied by the analytical expressions for the ideal two-dimensional hydrogen atom. Therefore. large momentum transfers are significantly suppressed and we expect that the spread of $\mathcal{S}^{(2)}_{\boldsymbol{q}nm}$ in momentum space is only on the order of the inverse exciton radius. We use this result to reduce the numerical effort in solving for correlation functions by replacing all quantities by their average over $\boldsymbol{q}$.

We also assume that the effective-mass approximation (EMA) applies within this region and that band anisotropy can be neglected. In this case, the internal and external motions of excitons decouple and wave functions become separable in the relative and total momentum variables. The correlation functions $\mathcal{P}^<_{\boldsymbol{q}nm}(t,t')$ can then depend on $\boldsymbol{q}$ via the center-of-mass kinetic energy of the exciton, $\hbar\Omega_q=\hbar^2q^2/2M$. Furthermore, within the EMA, the matrix elements $A_{nm}(\boldsymbol{q},\boldsymbol{q}')$ also depend only on the difference of momenta, i.e., the momentum transferred and not how fast the exciton moves in initial and final states. Thus the superoperator $\mathcal{C}$ has the simpler form

$$\mathcal{C}_{mn;m'n'}(\boldsymbol{q},\boldsymbol{q}'|\tau,\tau')=\mathcal{C}_{mn;m'n'}(\boldsymbol{q}-\boldsymbol{q}'|\tau)\mathcal{P}^>_{\mathrm{Q};\boldsymbol{q}nn}(\tau'),$$

where

$$\mathcal{C}_{mn;m'n'}(\boldsymbol{q}|\tau)\equiv iW^<_{\mathrm{Q}}(\boldsymbol{q}|\tau)A_{mm'}(\boldsymbol{q})A_{n'n}(\boldsymbol{q}).$$

Apart from the factor $\mathcal{P}^>_{\mathrm{Q};\boldsymbol{q}nn}(t''-t_2)$, the integral over $\boldsymbol{q}'$ in Eq. (42) becomes a convolution. By switching to the interaction picture with respect to $\Omega_{\boldsymbol{q}}$, the main contribution of $\mathcal{P}^>_{\mathrm{Q};\boldsymbol{q}nn}(t''-t_2)$ to the integrand in Eq. (42) is a factor $e^{i(\Omega_q-\Omega_{q'})(t_1-t'')}$. This can be taken to be unity to a good approximation, since the time difference t_1-t'' for which there is significant contribution is restricted by the inverse bandwidth of the kernel. The kinetic-energy transfer $|\Omega_q-\Omega_{q'}|$ will be large only for large values of q', which are expected to lie in the pair-excitation continuum and thus have a large bandwidth. Thus, $e^{i(\Omega_q-\Omega_{q'})(t_1-t'')}$ will deviate from only slightly from unity. In the preliminary study here, we neglect this deviation and introduce the exciton correlations traced over the total momentum states,

$$\mathcal{P}^<_{nm}(t,t')=\int\frac{d\boldsymbol{q}}{4\pi^2}\mathcal{P}^<_{\boldsymbol{q}nm}(t,t'),$$

and also define $\mathcal{S}_{nm}(t,t')$ as the result of a similar integration of $\mathcal{S}_{\boldsymbol{q}nm}(t,t')$.

Integrating over $\boldsymbol{q}$ in Eq. (42) and neglecting the kinetic energy of the exciton motion, we get

$$\begin{aligned}\left(\frac{\partial}{\partial t_1}+\frac{\partial}{\partial t_2}\right)\mathcal{P}^<_{nm}(t_1,t_2)+i[\mathcal{H},\mathcal{P}^<_{nm}(t_1,t_2)]-\mathcal{S}_{nm}(t_1,t_2)\\ =\int_{-\infty}^{t_2}dt''\mathcal{C}_{nm;n'm'}(t_1-t'',t''-t_2)\mathcal{P}^<_{n'm'}(t_1t'')\\ -\mathcal{P}^<_{nm'}(t_1t'')\mathcal{B}_{m'm}(t''-t_2)+\int_{-\infty}^{t_1}dt''\mathcal{C}_{nm;n'm'}(t''-t_2,t_1\\ -t'')\mathcal{P}^<_{n'm'}(t''t_2)-\mathcal{B}_{nn'}(t_1-t'')\mathcal{P}^<_{n'm}(t''t_2).\end{aligned} \tag{47}$$

Similarly, we define $\rho_n(t)$ be equal to $\rho_{\boldsymbol{q}n}$ summed over all $\boldsymbol{q}$ and obtain

$$\left(\frac{d}{dt}+i\omega_n\right)\rho_n(t)=U_n(t)+\int_0^\infty d\tau\mathcal{B}_{nm}(\tau)\rho_m(t-\tau). \tag{48}$$

Here, $\mathcal{C}$ and $\mathcal{B}$ represent the integration of Eqs. (43) and (44) over the momentum arguments, while the relation between $\mathcal{C}$ and $\mathcal{B}$ in the new form is

$$\mathcal{B}_{mm'}(\tau)=\sum_j\mathcal{C}_{jj;m'm}(-\tau,\tau). \tag{49}$$

Note that due to the assumption of isotropic bands, the elements $\mathcal{C}_{nm;n'm'}$ are nonzero only if the difference in parity between n and n' is the same as that between m and m'.

Equation (48) has the formal solution

$$\rho_n(t)=\int_0^t dt'\psi_n(t-t')U_n(t'), \tag{50}$$

where $\psi_n(t)$ is the solution obtained by replacing $U_n(t)$ by $\delta(t)$. We write the Laplace transform of a function $f(t)$ as $\hat{f}(z)$ and obtain the Laplace transform of $\psi_n(t)$ in the form

$$\hat{\psi}(z)=[zI-\hat{\mathcal{B}}(z)]^{-1},$$

where I is the identity matrix of the same dimension as $\mathcal{B}$. In the case of $2s$ and $2p$ superpositions, the use of isotropic model, and the neglect of coupling to states of principal quantum number $n\neq 2$, the matrix $\mathcal{B}(\tau)$ becomes diagonal. In

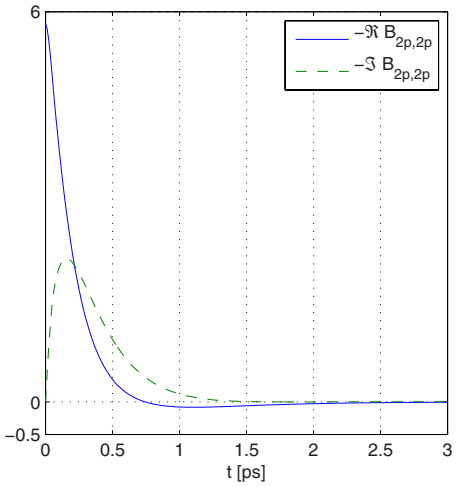

FIG. 4. (Color online) Typical $\mathcal{B}_{nn}(\tau)$.

the following sections, we discuss the calculation of $\mathcal{B}(\tau)$, but it is convenient to use the result obtained there in the present analysis. As shown in Fig. 4, the shapes of functions $\mathcal{B}_{nn}(\tau)$ are close to damped exponentials and thus may be approximate as the functions $-b_n e^{-\gamma_n t}$, where γ_n lie in the right half complex plane. Then the Laplace transform may be inverted to obtain

$$\rho_n(t) = \int_0^t dt' e^{-\gamma_n t'/2}\left[\cosh(\beta_n t') + \frac{\gamma_n}{\beta_n}\sinh(\beta_n t')\right] U_n(t-t'),$$

$$\beta_n \equiv \sqrt{\frac{\gamma_n^2}{4} - b_n}. \tag{51}$$

This simple formula is useful in explaining the behavior of $\rho_n(t)$ determined by numerical calculation.

When short pulses of less then 100 fs are used, the functions multiplying $U_n(t-t')$ in Eq. (51) may be taken out of the integral and evaluated at $t'=t$. Thus we expect two rates of decay that are mixed together after convolution with the optical pulse. The temporal behavior naturally approaches Markovian at times beyond few time constants of the faster decay rate but only if $\Im\beta_n$ vanishes. The system becomes manifestly non-Markov for large values of b_n, which corresponds to large coupling to the dynamical environment. Similarly, a small $|\gamma_n|$ also results in non-Markov behavior, which is due to the coupling to fewer modes of the environment and therefore a slower rate at which the phase information is lost.

We now turn to the two-particle equation (47). At first, for purely pedagogical reasons, let us consider only the diagonal terms in both $\mathcal{C}$ and $\mathcal{B}$ so that the integrand in Eq. (47) takes the form

$$= -\frac{1}{2}\int_0^\infty d\tau\left[\int dq i W_{\mathrm{Q}}^<(q,\tau)\{A_{mm}(q) - A_{nn}(q)\}^2\right]\{\mathcal{P}_{nm}^<(t,t-\tau) + \mathcal{P}_{nm}^<(t-\tau,t)\} - \frac{1}{2}\int_0^\infty d\tau\left[\int dq i W_{\mathrm{Q}}^<(q,\tau)\{A_{mm}^2(q) - A_{nn}^2(q)\}\right]\{\mathcal{P}_{nm}^<(t,t-\tau) - \mathcal{P}_{nm}^<(t-\tau,t)\}. \tag{52}$$

By the relation $\mathcal{P}^{<\dagger}(tt') = \mathcal{P}^<(t't)$, the first term plays the dominant role in decay of $\mathcal{P}_{nm}$, while the second contributes to oscillations. Analogous formula for Eq. (48) reads

$$-\frac{1}{2}\int_0^\infty d\tau\left[\int dq i W_{\mathrm{Q}}^<(q,\tau)A_{nn}^2(q)\right]\rho_n(t-\tau). \tag{53}$$

Thus the rate of decoherence of each state with the ground state depends on how strongly the state scatters the surrounding quasiparticles. On the other hand, the factor $A_{mm}(q) - A_{nn}(q)$ in Eq. (52) shows that their decoherence with respect to each other depends on *how differently* they scatter the quasiparticles. Therefore, states that decohere at a very fast time scale may continue to be coherent with each other if their spatial profiles are such that their multipole moments are similar. Similarly, if the rates are vastly different, the mutual decoherence will be only slightly less than the faster decay rate of interband polarizations. Note that in both cases, one or both interband polarizations can completely vanish while a substantial mutual coherence remains. This is verified in the numerical calculations below.

In general, the off-diagonal terms in $\mathcal{C}$ are also important. However, they involve overlaps between eigenfunctions of different energies, which tend to be smaller. Furthermore, due to the dominance of low frequencies in $W_{\mathrm{Q}}^<(\tau)$, the contribution of off-diagonal terms is also small on average when Eq. (47) is integrated. This is confirmed in our numerical calculations below.

We now turn to the conditions that determine how far the system is from Markov dynamics. It is obvious from the integrals in Eq. (47) that the width of $\mathcal{C}(\tau,\tau')$ in its first argument, τ, controls how close the dynamical system is to being Markovian. This width is in turn controlled by the matrix elements $A_{nm}(q)$, which depend on the nature of the exciton states involved in scattering, and the function $W_{\mathrm{Q}}^<(q,\tau)$, which connects the static properties of these states to dynamics. The matrix elements $A_{nm}(q)$ can be expanded in an infinite sum over the multipole moments of the exciton. The profile for $A_{nm}(q)$ is broader and centered at larger momentum for more tightly bound states than for loosely bound states. The dielectric function generally has sharper peaks in the frequency domain at smaller q owing to the presence of the plasmon branch at low momenta. At higher frequencies where there is a continuum of particle-hole excitations, the correlation functions $W_{\mathrm{Q}}^<(q,\omega)$ acquire a broad frequency distribution. As a result, virtual excitations among lower energy, more tightly bound states, will have broader spectra or, in other words, will be closer to Markov than the higher-energy states.

Furthermore, only very fast quasiparticles of the background gas will significantly scatter from tightly bound states. If such a quasiparticle has a velocity u_q, then it will typically interact with the state of size a for a time $\sim a/u_q$, and for it to be effective in causing decoherence, the quantity $|\mathcal{C}|a/u_q$ must be significant. It follows then that the lower-lying states, besides being less affected by memory terms, also have slower decoherence rates due to their smaller size. In two-dimensions, the $(n+1/2)^{-2}$ dependence of energy levels enhances the size difference between the lowest and the

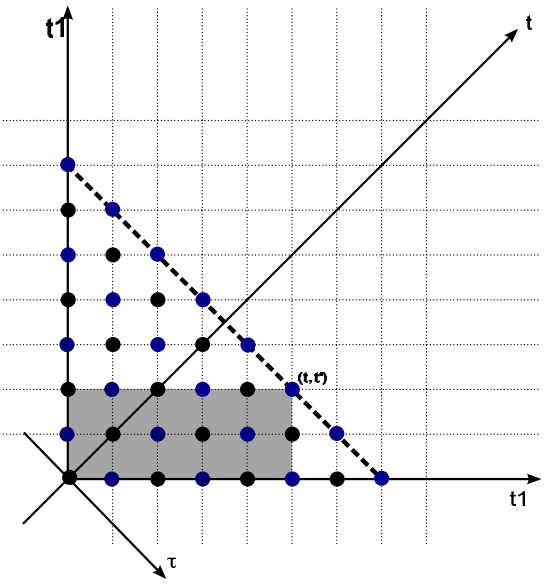

FIG. 5. (Color online) Two-time grid used in computation of Eq. (47). The dots on alternating antidiagonal lines (or black vs blue dots) form complementary subgrids. The shaded rectangle is domain of memory integral contributing to the point (t,t') at its top right corner. Thick dashed line indicates the "front" on which all points are calculated by linear multistep method from the previous front of the same subgrid.

second-lowest states of excitons, which makes a pronounced difference in their decoherence behavior as well.

It is worth noting that the integral limits in Eq. (47) force the domain of integration to be the horizontal and vertical lines whose one end point is the point where the solution is sought (see Fig. 5). In the more general equations (38), this point lies on the same lines but there is also an additional contribution from the line connecting the point to the line, $t_1=t_2$. The additional integration accounts for excitation induced effects in the evolution of the exciton removal amplitudes. In other words, it describes the deviation in the evolution of the exciton population and is zero by assumption of vanishing hole density in the background state. In the exact treatment, but still keeping the initial hole density zero, this contribution will account for the EID and relaxation effects. Its absence here allows us to solve Eq. (47) with explicit propagation only along $t=(t_1+t_2)/2$, which then implicitly leads to dependence on $\tau=t_1-t_2$ via the memory integrals only.

The neglected EID can be accounted for by a resummation, where the bubble diagrams comprising the density response function are corrected by the induced carrier density. The main effect of this will be the much broader spectral response because the rate of change of the density is of the order of the pulse width and hence subpicosecond. Due to the fact that the equilibrium gas interacts very weakly with the $1s$ exciton state, the latter is expected to decohere from the semiconductor vacuum mainly via EID. This is roughly due to the fact that the equilibrium density response is sharply suppressed at large energy, which also severely limits the momentum transfer. All these effects act against $1s$ decoherence. On the other hand, EID may provide enough spectral range to couple into the large energy transfers and thus allows the intermediate transitions from $1s$ to all the states lying above it. This coupling may be the dominant source of decoherence of $1s$ state. However, the $2s$ and higher states are dephased quickly by the equilibrium gas alone and EID is therefore expected to affect them only quantitatively. Below, we perform calculations for $2s$ and $2p$ states and we will leave decoherence of $1s$ state to future publications.

We conclude this section by drawing comparison of our approach and its results to the conventional system-bath models that would treat the electron gas as distinguishable from the exciton. The two-time correlation function in our model is in direct contrast to single-time density matrices used in system-bath models. Different contour orderings of the former generate correlation functions describing different types of excitations in the multielectron system. In Eq. (38), we see that the exciton correlation function $\mathcal{P}^<$ is coupled to the correlation functions $\hat{\mathcal{P}}^{\pm}$ and $\check{\mathcal{P}}^{\pm}$, the spectrum of which corresponds to excitations in the $N\pm1$ particle Hilbert space. These correlations are related to the composite nature of the exciton. While this arises naturally in the present model, these different types of excitations would have to be introduced phenomenologically in a system-bath model that treats exciton as distinguishable from the rest of the electronic system. The present model is also in a form in which a preexisting population of excitons can be taken into account self-consistently.

Another important difference between the present model and the system-bath models is the presence of source terms in Eq. (42). These source terms result from treating exciton as part of a fully quantum-mechanical multiparticle system, as is clear from their relation to the effective interactions and the single-particle self-energy. Also, the source terms and the couplings ultimately originate from a single equation: the Dyson equation. On the other hand, a conventional system-bath model describes only the evolution of a density matrix, the preparation of which is outside the realm of the model. Such a treatment cannot account for the simultaneous generation and dephasing of excitons as is done in the present model. Given the relatively long time scales of decoherence compared to the ultrashort pulses in systems such as the one being studied, treating the generation and dynamics of excitons at the same footing is indeed important.

V. NUMERICAL METHOD

We now turn to the numerical calculations of Eqs. (47) and (48). To proceed, we need to compute the superoperators $\mathcal{C}(\tau,\tau')$, which depend on $W_{\mathrm{Q}}^<(\boldsymbol{q},\tau)$ as shown in Eq. (43). The KMS relations yield the Fourier transform of $W_{\mathrm{Q}}^<(\boldsymbol{q},\tau)$ in the form

$$iW_{\mathrm{Q}}^<(\boldsymbol{q},\omega) = -\int_{-\infty}^{+\infty} \frac{2V(q)\Im\varepsilon^{-1}(\boldsymbol{q},\omega)}{e^{\beta\omega}-1}.$$

In this section, we first discuss the model used in computing relevant properties of the electron gas, including the inverse dielectric function $\varepsilon^{-1}(\boldsymbol{q},\omega)$. We then describe our time-

stepping scheme for solving the dynamical equations.

A. Electron gas

We model $\varepsilon^{-1}(\boldsymbol{q},\omega)$ by setting its imaginary part equal to that given by the Lindhard formula. At very small q, the plasmon branch appears and leads to very sharp peaks that we handle by replacing $\varepsilon(q,\omega)$ by the single plasmon pole model for small q,

$$\Im\varepsilon^{-1}(q,\omega) = \frac{\omega_{pl}^2}{2\omega_q}\left[\frac{1}{(\omega+\omega_q)^2+\gamma_q^2} - \frac{1}{(\omega-\omega_q)^2+\gamma_q^2}\right],$$

where ω_q is the energy of plasmon at wave number q and γ_q is its decay rate. The real part can be calculated by Kramers-Kronig relation and its zero-frequency limit relates the static screening to plasmon dispersion at small q, i.e.,

$$\omega_q^2 = \omega_{pl}^2(q)\left(1+\frac{q}{\kappa}\right) - \gamma_q^2.$$

Here, κ is the screening parameter and we took the nominal dielectric constant to be 13. Independent of the temperature, the RPA calculation will produce $\gamma_q \to 0$ in the limit $q \to 0$ so that the above formula makes sense as $\omega_{pl}^2 \to 0$ in two dimensions in the same limit. We set temperature equal to 10 K in calculations.

With the above model for the dynamical potential, we computed γ_q self-consistently with the quasiparticle energy shifts, which are equal to the real part of the retarded self-energy. We took the latter within the GW approximation, as is consistent with the assumptions of Appendix C,

$$\Sigma^r(\boldsymbol{k},t) = \frac{i}{8\pi^3}\int d\boldsymbol{q}\int d\omega' W^r(\boldsymbol{q},\omega')G^r(\boldsymbol{k}-\boldsymbol{q},\omega-\omega').$$

This energy shift is decomposed into two parts: the larger static part, $\Sigma_s(k)$, and the smaller shift, $\Sigma_d(k) = \Re\Sigma^r[k,E(k)] - \Sigma_s(k)$, which arises from the dynamical self-energy. Within the GW approximation and at densities and temperatures involved, we found that $\Sigma_d \ll \Sigma_s$ and could therefore be neglected. These calculations were performed by ignoring the quasiparticle broadening in the integrals. The results support this neglect because the on-shell imaginary self-energy, $\Im\Sigma^r[k,E(k)]$, is almost 1 order of magnitude smaller than γ_q for small k, where the energy shifts are the largest.

B. Numerical time stepping

We obtained the numerical solution of Eq. (48) by using the fourth-order backward-differentiation formula (BDF).[27] We applied this to both the time stepping and the memory integral. While other quadrature schemes (trapezoidal and Simpson rule as well as second-order BDF) also produced results that agreed with the fourth-order BDF, they required smaller time steps and became unstable after fewer time steps than the fourth-order BDF.

We used the same quadrature scheme for the numerical solution of Eq. (47) in the two-dimensional time plane. To describe the numerical algorithm briefly, we begin by making a change of variables to $T=(t+t')/2$ and $\tau=t-t'$ and denote a two-time function, $\mathcal{F}$, in terms of these variables $\tilde{\mathcal{F}}(t,\tau)$. The two-dimensional time plane was divided into lines (referred to as fronts hereafter) along which τ varied at a fixed T. The memory integrals in Eq. (48) are such that only the information to the left of the front is necessary to propagate the solution. A square grid in the (t,t') plane was used and the above scheme partitions it into two mutually exclusive subgrids—one containing the diagonal $t=t'$ and the one that does not. Propagation was performed by alternating the propagation of the fronts on each subgrid as depicted in Fig. 5.

It is necessary to restrict the maximum value τ_{max} of $|\tau|$ to compute a solution with reasonable memory requirements. We chose τ_{max} by trial and error and thus obtained a solution in a strip of finite width centered at $t=t'$. Due to the finite memory time of the kernels, the strip can be much longer than its width. Thus a grid large enough to contain the width can be translated parallel to $\tau=0$ line when computing the full dynamics. We increased τ_{max} from one memory width until the solution converged, which occurred for τ_{max} larger than about five memory widths. Smaller values τ_{max} introduced divergence in the tail of the graphs. This is due to the buildup of errors at the edge of strip, which propagate via the memory integrals back to the time diagonal.

Finally, we performed the two-dimensional Fourier transforms by fast Fourier transform (FFT) on the function $\tilde{\mathcal{P}}^<(t,\tau)$. We applied an envelope function $1-|\tau|/\tau_{max}$ to prevent spurious oscillations for FFT along the antidiagonals in the two-time plane. This modification preserved the shape of the plots but removed extremely fast oscillations due to the Gibbs phenomenon arising from a steplike behavior at the edges of the strip.

VI. RESULTS

Figure 6 shows the behavior of the energies of exciton states as a function of the density. The lowest-lying $1s$ state is far below and is not shown. The p and s states at low density merge toward their ideal values $(n+1/2)^2$ Ry, while the effect of static screening with increasing density is to make the p states rise above s in energy. All states merge into the continuum as density is increased, where the continuum itself is lowered by the Hartree-Fock self-energy. The lines in the figure show the effect of only the static self-energy correction, while the green dots show the results of a few calculations done with the dynamical self-energy included. Clearly the dynamical effects on these energies are too small and were neglected in calculating the kernels.

The energy of the $1s$ state lies below -3 Ry (1 Ry ≈ 5.23 meV) for densities below $2\times10^{-3}a_0^{-2}$. Here, a_0 is the Bohr radius in the zero-screening limit using the dc dielectric constant of GaAs. Its value is 10.58 nm. We perform calculations with the $2s$ and $2p$ states in the model without spin splitting. The energy diagram shows that the continuum is lowered significantly at $2\times10^{-3}a_0^{-2}$ and above this density, the wave functions of $n=2$ states start to be dominated by mixing from the scattering states.

We note that the energy difference between the continuum and the $2p$ state is approximately 0.1 Ry at $n_c=2\times10^{-3}a_0^{-2}$,

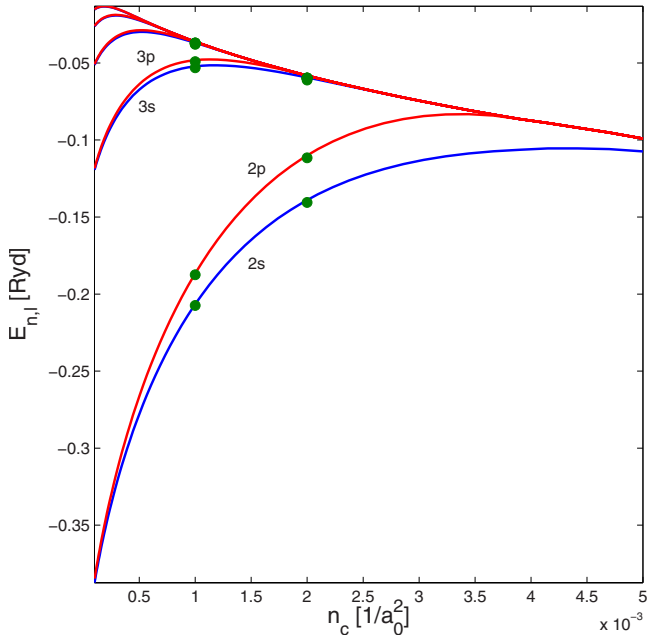

FIG. 6. (Color online) Exciton energies vs electron gas density n_c. Calculation includes static Hartree-Fock correction. Red lines for p states and blue lines for s states. Green dots are from the dynamical corrections.

so that a pulse width of greater than 2 ps is required to keep the magnitude of excitations into the conduction band low. Since the density in the conduction band is proportional to the intensity, while the interband polarizations are proportional to the amplitude, the effects of density are not significant for much shorter pulses so long as the field is weak enough. However, this restriction can be relaxed further by pulse shaping and by shifting the center frequency of the pulse deep into the band gap. In the latter case, the ratio of the intensity at the conduction-band edge to the amplitude at the $2p$ pulse decays rapidly.

We now discuss the results of solving the equation of motion (48) via the numerical procedure described above. Figure 7 shows the coherence, $\rho_n(t)$, between the ground state and the $2s$ and $2p$ exciton states. Graphs are shown at two different pulse widths and two different densities. On the left are graphs for pulse width of 0.0625 ps and on the right the pulse width is 0.5 ps. The top row corresponds to the density of $n_{c1}=10^{-3}a_0^{-2}$ $(9\times10^9\ \mathrm{cm}^{-2})$ and the bottom row shows the results for twice this density (called n_{c2} hereafter). The pulse envelope function is superimposed as dashed line but it is not to scale.

In both cases, the coherence remains for the same duration of approximately 16 ps much longer than the pulse. The transient effects of the pulse remain for longer than the pulse width due to memory. The memory, or the temporal width of $\mathcal{B}_{nm}(\tau)$, is approximately 1 ps for both densities. The response to the shorter pulse shows three regimes of decay.

The first regime following the peak is marked by an approximately linear drop in $\rho_n(t)$. The slopes of the curves in this regime are approximately -1.5 and -2.5 at n_{c1} and n_{c2}, respectively. The third regime, or the tail end of $\rho_n(t)$, is predominantly exponential. The exponential decay rates for n_{c1} and n_{c2} do not differ much and thus the decoherence rate grows sublinearly with density despite the linear growth of the amplitude of $\mathcal{B}_{nm}$ with density. The intermediate regime is not described by a simple power law or an exponential decay since it is affected by all the decay rates.

We now turn to the results obtained by solving for the exciton correlation $\mathcal{P}^<(t,t')$ via Eq. (47) and shown in Fig. 8 along the line $t=t'$ in the two-time plane. The solid curves show the matrix elements $\mathcal{P}^<_{nm}(t,t)$, while the dashed lines show the driving terms, $\mathcal{S}(t,t)$, along the same line in two-time plane. The interband coherence has almost the same behavior as the driving term, as expected. By comparing the left and right columns, we note that the amplitude of $\mathcal{S}$ scales approximately linearly with density. This is consistent with the fact that the source is driven by the dynamic part of the potential and two factors of this scale as the first power of density.

The top row in Fig. 8 shows $\mathcal{P}^<_{2p,2s}(t,t)$, which is the coherence between the $2s$ and $2p$. Clearly, the decoherence is weak enough that $\mathcal{P}^<_{2p,2s}(t,t)$ remains significant for time much longer than the duration of the interband coherence and the driving term. The approximate exponential decay following the peak, and the slowly decaying tail of the curves, indicates the presence of several different rates in the dynamics of $\mathcal{P}^<_{2s,2p}(t,t)$.

To investigate further, we introduce time-dependent rates

$$\gamma_n(t) = -\frac{d}{dt}\log|\rho_n(t)|,$$

$$R^0_{nm}(t) = -\frac{d}{dt}\log|\rho_n(t)\rho^*_m(t)|,$$

$$R_{nm}(t) = -\frac{d}{dt}\log|\mathcal{P}^<_{nm}(t,t)|,$$

such that these functions would be constant for a purely exponential decay or Markov behavior. The function $R^0_{nm}(t)$ is essentially the sum of decoherence rates for the two interband polarization amplitudes involved and thus it represents the decay rate of the noninteracting approximation to the Green's function (7). The function $R_{nm}(t)$ isolates the rates associated with the terms beyond the free Green's function. Based on these rates, a phenomenological measure of correlation can be introduced, in analogy to that by Ferrio and Steel.[13] We let $\mathcal{Q}_{nm}(t)$ be such that

$$R_{nm}(t) = \gamma_n(t) + \gamma_m(t) + 2\mathcal{Q}_{nm}(t)\sqrt{\gamma_n(t)\gamma_m(t)}. \qquad (54)$$

A large magnitude of $\mathcal{Q}_{nm}(t)$ corresponds to large contribution of the correlation $X^{(2)}_{cvvc}$ to G_{cvvc} in Eq. (6). A positive value of $\mathcal{Q}_{nm}(t)$ indicates a stronger decoherence among the exciton states compared to that of interband polarization. On the other hand, a value of $\mathcal{Q}_{nm}(t)$ close to -1 indicates that $R_{nm}(t)$ is approximately the square of the difference of the decay rates of interband polarization. Thus, $\mathcal{Q}_{nm}$ summarizes the relationship between the decoherence between excited states and the decoherence of these states with the ground states. Figure 9 shows $\mathcal{Q}_{nm}(t)$ for the two calculations and its values are indeed close to -1. The detailed behavior of

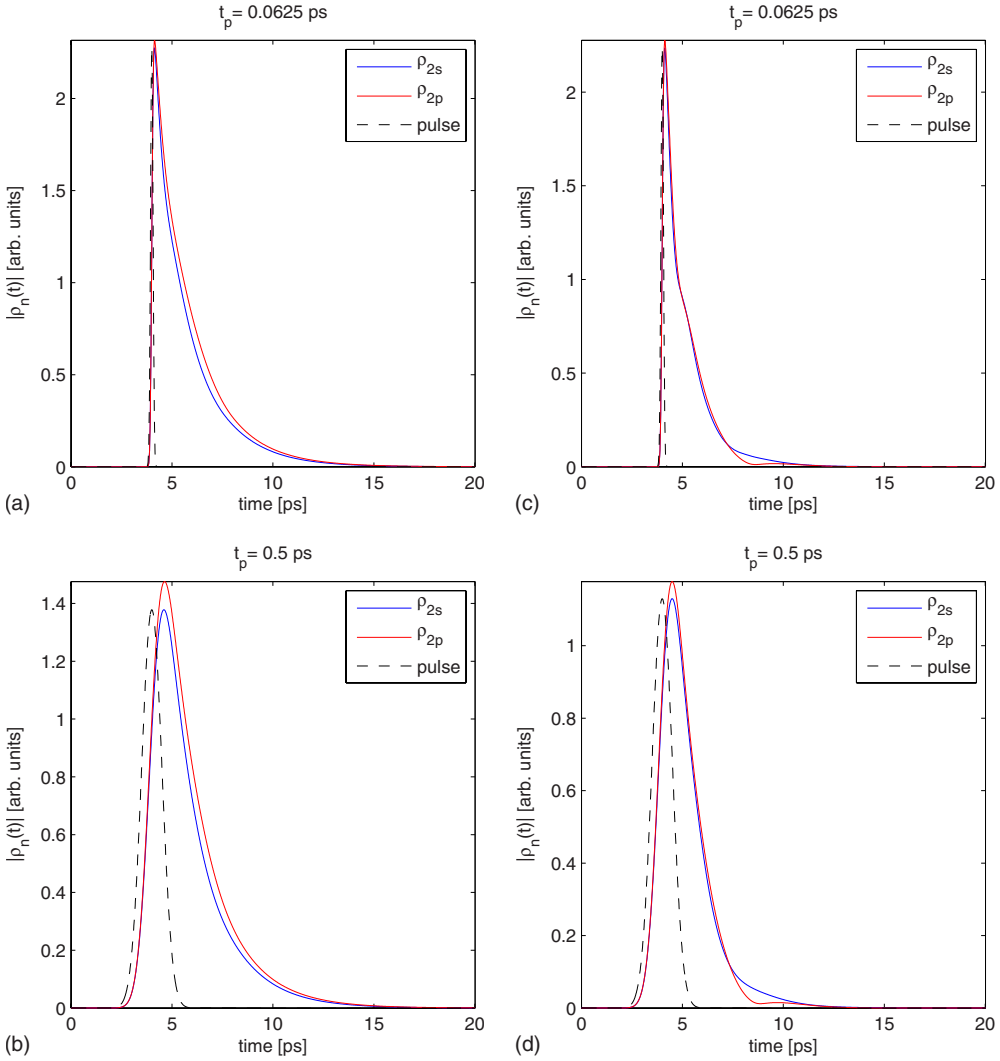

FIG. 7. (Color online) Interband polarizations for the $2s$ and $2p$ states at two different pulse widths. Densities are $n_c=10^{-3}a_0^{-2}$ (top) and $n_c=2\times10^{-3}a_0^{-2}$ (bottom).

$\mathcal{Q}_{nm}(t)$ is more easily understood from that of R^0_{nm} and R_{nm}, to which we now turn.

Figure 10 shows the plots for these two functions based on the calculations presented above. It is immediately clear that the $R_{nm}(t)$ is 1 order of magnitude less than $R^0_{nm}(t)$. The decoherence rates rise sublinearly with respect to density as is evident by comparing the rates in the free evolution regime for both R^0 and R. The oscillations in $R^0_{nm}(t)$ can be understood as bath-induced effects in the dynamics of $\rho_n(t)$. The simple analytical solution (51) shows that at larger densities, b_n increases and eventually makes the effective shift in the rates, β_n, complex. Since solutions include both β_n and $-\beta_n$, the oscillations continue to exist in $|\rho_n(t)|$.

Turning now to the function R, we note that it has several rates, including very low ones that dominate the tail of the coherence. The latter would be superseded by other processes that begin to appear on time scale of tens of picoseconds. There is a steep transition between the decay rate of the intermediate regime that follows the pulsed excitation and the one in the long time limit. The rates in each regime vary by only a few percent, where the are plateaus in the function $R_{nm}(t)$ at both densities. One could associate a short-ranged Markov behavior in these regimes. The sharp transition is partly due to the slow oscillation in the real and imaginary parts of $\mathcal{P}^<_{nm}(t,t)$; the period of this oscillation is similar to the time over which the slow decay takes over from the fast decay of $R_{nm}(t)$.

Finally, we discuss the two-dimensional plots of the signal that results after interaction with a third pulse. As mentioned at the start of Sec. III, we take the first two pulses to be coincident [$t_b=0$ in I-(110)] and perform the Fourier transform of the numerically solved function $\tilde{\mathcal{P}}^<(t,\tau)$ as discussed in Sec. V above. Recall from I that the two-dimensional Fourier transform is applied to the function $\tilde{\mathcal{P}}^<(t_d+\tau/2,\tau)$, where t_d is the time between the first two pulses and the third pulse. Keeping the same notation as in I, the variable ω is conjugate to the time t_d and Ω to τ. The variable τ maps directly to the difference time so that for a fixed t_d, the Fourier transform from τ to Ω is related to the spectrum of the exciton levels. The spectrum evolves as the variable t_d changes such that the point (t_d,Ω) represents the spectrum for which t_d is the time at which electron-hole pair

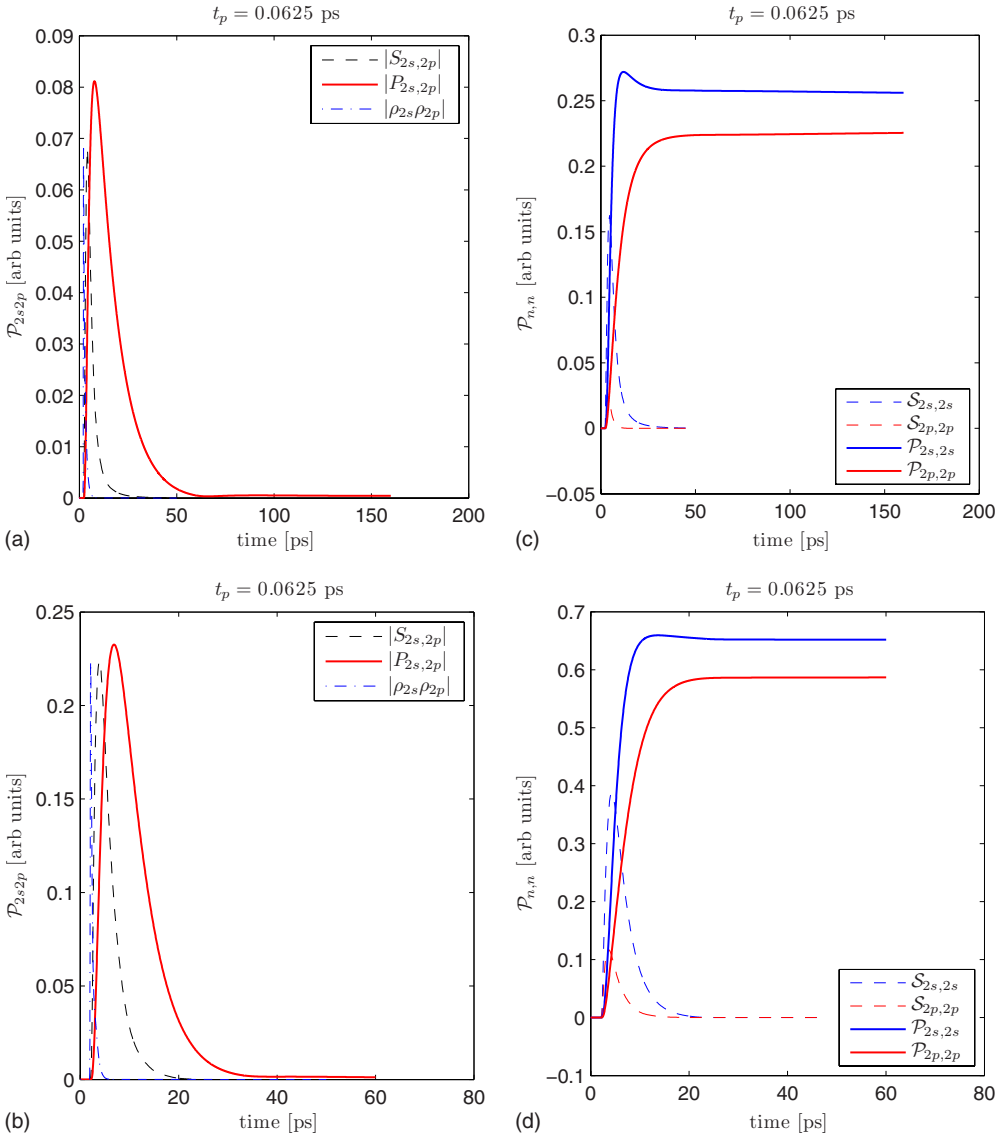

FIG. 8. (Color online) Coherence (top) between the $2s$ and $2p$ states of $\mathcal{P}^{<}(t,t)$ at densities $n_c = 10^{-3}a_0^{-2}$ (left) and $n_c = 2\times 10^{-3}a_0^{-2}$ (right). The bottom row shows the populations of the respective levels. The source terms are superimposed as dashed curves and its duration is about the same as interband polarization.

begins propagation. Since the time of measurement follows the third pulse, the Fourier transforms are computed only in the region $t_1 \geq t_2$ or for $\tau > 0$. Therefore, the functions $\tilde{\mathcal{P}}^{<}_{nm}(t,\tau)$ describe the overlap at time $t+\tau/2$ between state with exciton in level n removed and the state from which an exciton in level m is removed a time τ earlier.

Figures 11 and 12 show the two-dimensional Fourier transforms at densities n_{c_1} and n_{c_2}, respectively. In the left-hand panels are the driving terms and in the right-hand panels are the solutions. While only the solutions constitute experimental predictions, we have included the driving terms to identify the features of the solutions originating from them, as opposed to the dynamical map. This would clarify the properties that $\mathcal{P}^{<}_{nm}$ inherit from interband polarization and what effects the dynamical map has on them.

As discussed in Sec. III A 2, the contributions of $\mathcal{P}_{2s,2p}$ and $\mathcal{P}_{2p,2s}$ are separated spatially at the detector. The figures show these contribution matrix elements in separate windows.

The peaks are in proximity of the expected locations, $(\Omega,\omega) = (\omega_n, \omega_{nm})$, with a slight overall shift along the Ω axis, and the shift is almost equal in both the source and the solution plots. Thus they are largely due to the oscillations in the source term and appear in $\mathcal{P}_{nm}$ as a result of being driven by the source terms. That the dynamical map makes negligible contribution to the shifts is also consistent with the fact that dynamical corrections show little effect in the exciton energy levels of Fig. 6. We define the peak location along this axis by the first moment of the absolute value squared of the corresponding function. The shifts at higher density are slightly larger and the peak for $\mathcal{P}_{2p,2s}$ shifts in the positive direction while the peak for $\mathcal{P}_{2s,2p}$ shifts to the negative direction and by a smaller amount. The spread in the Ω direction in both driving terms and solution is also similar. This is due to the fact that excitation-induced changes in the exciton

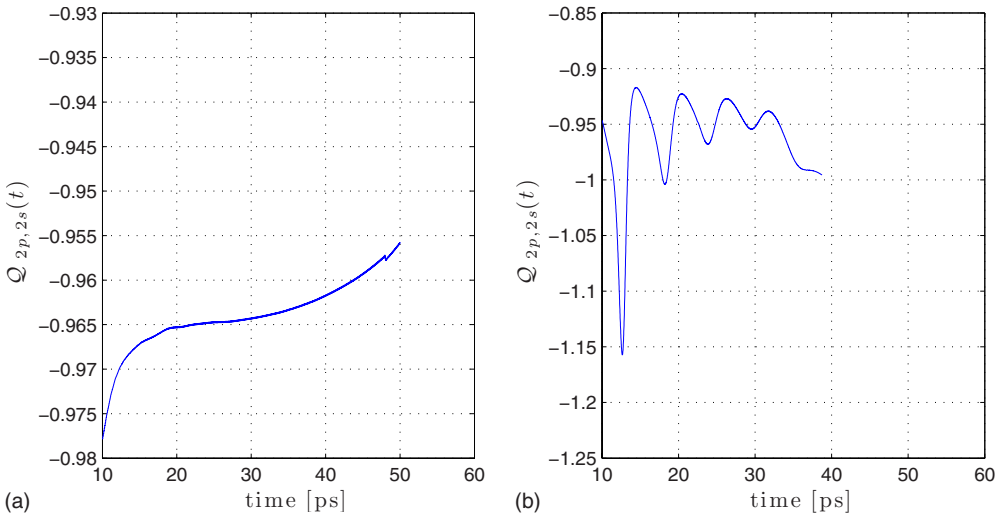

FIG. 9. (Color online) Phenomenological parameter $\mathcal{Q}$ corresponding to the plots in Fig. 8 [densities $n_c=10^{-3}a_0^{-2}$ (left) and $n_c=2\times10^{-3}a_0^{-2}$ (right)].

spectrum show up as deviations in the propagation of the exciton population. As was discussed at the end of Sec. IV, these effects occur either in the presence of initial exciton population or if excitation induced effects are somehow taken into account. Both are neglected in these calculations.

Another aspect common to both the $\mathcal{S}_{nm}$ and $\mathcal{P}_{nm}$ is the asymmetry in the magnitude of the functions; $\mathcal{P}_{2s,2p}$ and $\mathcal{S}_{2s,2p}$ are smaller than $\mathcal{P}_{2p,2s}$ and $\mathcal{S}_{2p,2s}$, respectively. This result is more naturally understood from the perspective of $\mathcal{P}$ than $\mathcal{S}$. The function $\mathcal{P}_{2s,2p}$ corresponds to removing a $2p$ exciton first, which leaves the $2s$ state to propagate for the time delay τ. The overlap is taken with a state from which the $2s$ exciton is removed, which in the presence of $2s-2p$ coherence is predominantly p-like. Since $2s$ state is already symmetric, evolution for time τ has little effect on its small overlap with a p-like state. On the other hand, in the function $\mathcal{P}_{2p,2s}$, the $2s$ exciton is removed first and thus the p-like remaining state is driven to a more symmetric form via interactions with the electron gas. The resulting state has higher overlap with the s-like state that arises from removing a $2p$ exciton. Thus indeed, we expect the $\mathcal{P}_{2s,2p}$ to be of lower magnitude than $\mathcal{P}_{2p,2s}$ when the Fourier transforms are performed only with $\tau\geq0$. The source terms $\mathcal{S}$ contain this property through the functions $f_{nn'}^{\zeta\zeta'}(\boldsymbol{q},\boldsymbol{q}',\tau)$ that describe how faithfully the exciton state n' evolves into n after time τ and momentum exchanges $\boldsymbol{q}$ and $\boldsymbol{q}'$.

Finally, the most obvious effect of the dynamical map is that the spread of the peaks along ω axis is greatly reduced from the source to the solution term. This reduction is much greater at lower density than it is at higher density, as expected. The non-Markov behavior can also be seen from the profile of the peak along ω for the Wigner function, $\tilde{\mathcal{P}}(\omega,\Omega)$. A pure exponential decay of Markov behavior would have ω dependence of the form $[\gamma^2+(\omega-\omega_0)^2]^{-1}$ that is symmetric about the center frequency. The profiles of the solutions $\tilde{\mathcal{P}}_{2p,2s}$ at the two densities are shown in Fig. 13. The curves are generally asymmetric around their respective peaks. The curves close to the center of the two-dimensional peak are more symmetric and therefore correspond to oscillators that evolve via smaller memory effects.

VII. CONCLUSION

We have presented an application of the formalism we developed for multidimensional Fourier spectroscopy of semiconductors.[12] The discussion in the present paper is centered on the dynamics of excitons and how it can be accessed in detail using a three-pulse optical excitation. We have shown how the interband coherence is transferred to the exciton correlation function, which can dominate the Raman coherence. This dominance is confirmed in the particular case of $2s$ and $2p$ exciton states that we considered. We remark that the signal generated by the third-order polarization can be viewed as the transfer of Raman coherence back to interband coherence. While the composite nature of the excitons is not relevant for decoherence in the parameter regime considered, we have presented the dynamical equations that allow for its treatment in more general problems.

The main analytical result is Eq. (47) for the correlation functions of exciton states, which may be thought of as a two-time generalization of a master equation. The interband polarization was found to be governed by Eq. (48), which is related to Eq. (47) in a physically transparent way. There is a reduction in the decoherence rate of an exciton if the two superimposed states have similar spatial properties. The decoherence of interband polarization is unaffected by this property because it addresses superposition with respect to the ground state.

Equation (47) and its interpretation presented above also connect directly to the conventional system-bath interaction, where decoherence results from the diminishing overlap of the two "final states" of the bath in an interaction process with the two superimposed states. However, the derivation of Eq. (47) makes no distinction between the system and the bath. The charge configurations characterize the different states of the "system" or the electron-hole pair and the approximation that leads only to the appearance of $A(q)$ re-

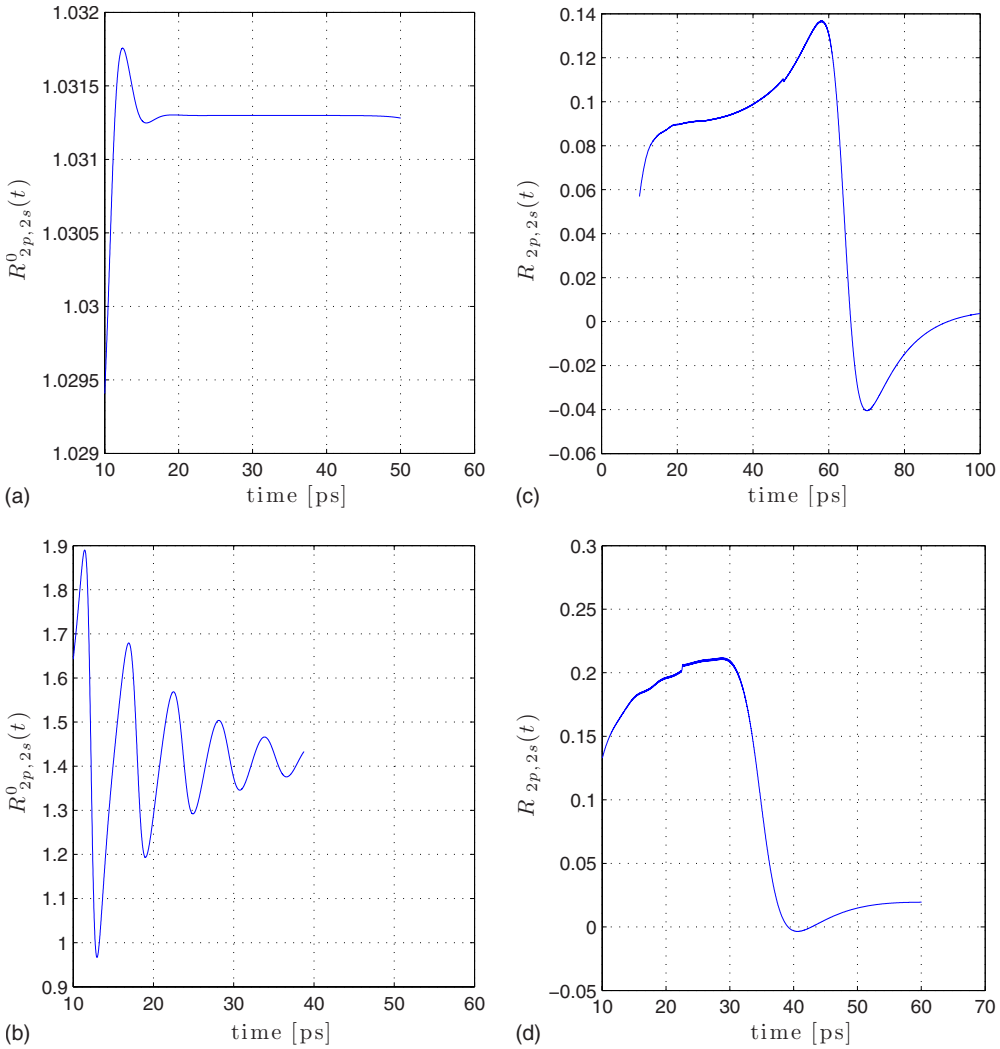

FIG. 10. (Color online) Comparison of $d \log f/dt$ where $f=\rho_n$, $\mathcal{P}^{<}_{nm}$ at densities $n_c=10^{-3}a_0^{-2}$ (left) and $n_c=2\times10^{-3}a_0^{-2}$ (right).

places these charge configurations by the multipole moments. Thus, the ability of "bath" of quasiparticles to *detect* a multipole moment of charge distribution maps directly to the decoherence of interband polarization and their ability to *distinguish* the two moments maps directly to the mutual decoherence of the two states.

In relating the dynamical equations to experimental scenarios, we found that a three-pulse excitation can, within the convolution effects of the third optical pulse, directly probe the two-time exciton correlations. This illustrates a powerful aspect of the two-dimensional Fourier spectroscopy. A reasonably direct access to the full temporal behavior of the two time functions allows one to compare theory and experiments in a way that allows various approximations and paradigms for describing these complex systems to be tested in great detail.

The numerical calculations confirm the main points of the analysis presented. In particular, the exciton decoherence rates were found to be much smaller than interband polarization. We also obtained plots of two-dimensional Fourier spectroscopy from our calculation of the two-time functions. These plots are the main link between experiment and theory. Their main qualitative features were explained and the slow decoherence rates were clearly identified by comparing the plots for the solution to those for the driving terms.

This purpose of this work was to expound the main features of the formalism, as well as to demonstrate the qualitatively different nature of coherences in optical excitation of the semiconductors. In future, the present set of equations should be studied in further detail and the nature of the composite functions should be identified. An interesting venue is to compute two-dimensional plots for various different models for the electron gas in order to determine how sensitive they are as a probe of the quasiequilibrium state. A step in this direction is to perform spectroscopy using time delay between the first two pulses. As pointed out in the text, this delay maps directly to the temporal behavior of the dynamic susceptibility of the electron gas.

ACKNOWLEDGMENTS

This work was supported by the Natural Sciences and Engineering Research Council (NSERC) of Canada. K.S.V. acknowledges support from NSERC. We thank S. T. Cundiff and members of his research group for many helpful discussions.

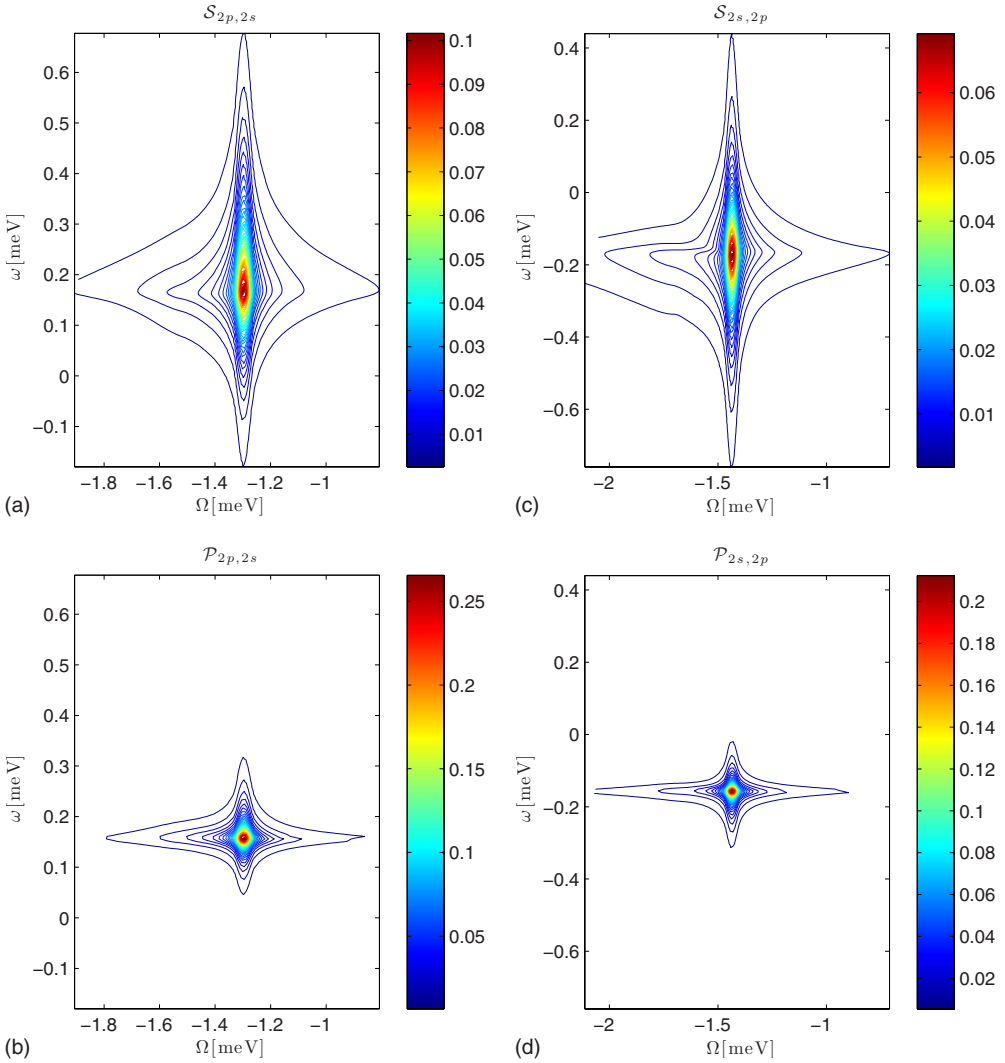

FIG. 11. (Color online) Two-dimensional plots showing absolute value of $\mathcal{S}_{2p,2s}$ and $\mathcal{P}_{2p,2s}$ at density $n_c=10^{-3}a_0^{-2}$.

APPENDIX A: KEY THEORETICAL QUANTITIES AND DEFINITIONS

In this appendix, we introduce the table listing the key quantities used in this paper and their correspondence with the notation of general formalism in I. The first column of the table lists each quantity in the notation of I. The two- and four-point functions are written in full notation even in the single and two-time limits, respectively, so that the link with the general formalism is clear. In order to maintain this relationship, we perform derivations in the notation of I and then recast the results in a simplified notation for brevity in the subsequent discussion. The second column introduces the corresponding symbols we use for brevity in this paper. The third column gives the key equation referring to the respective quantities. The fourth column gives a short summary of the context in which the quantity appears in the present theory. The third and fourth rows from the bottom list the result of the approximation scheme in the form of effective two-particle potentials for the exciton correlation function.

The effective potentials depend on the dynamical interaction $W(14;23)$, which is a two-time function in its most general form [see Eqs. (I-18) and (I-27)]. Its Keldysh matrix has the same properties as G and it is convenient to use the functions $W^{<}(tt')=W^{+--+}(14;23)$ and $W^{>}(tt')=W^{-++-}(14;23)$ in place of the four-point functions. Below, we use these functions evaluated at equilibrium and in this case they depend only on one time variable, the difference $t-t'$. We write them as $W_{\mathrm{Q}}^{\lessgtr}(\tau)$ and also introduce their Fourier transforms

$$W_{\mathrm{Q}}^{\lessgtr}(\omega)=\int_{-\infty}^{+\infty}d\tau W_{\mathrm{Q}}^{\lessgtr}(\tau)e^{i\omega\tau}. \tag{A1}$$

APPENDIX B: TWO-TIME APPROXIMATION

We use Eq. (15) to define the two-time *exciton Green's function* as

$$G_X(tt')\equiv G_{cvvc}(14;1^+4^+), \tag{B1}$$

such that the electrons are created and destroyed in pairs. The branch indices produce a 4×4 matrix $\hat{\boldsymbol{G}}_X(tt')$ in the

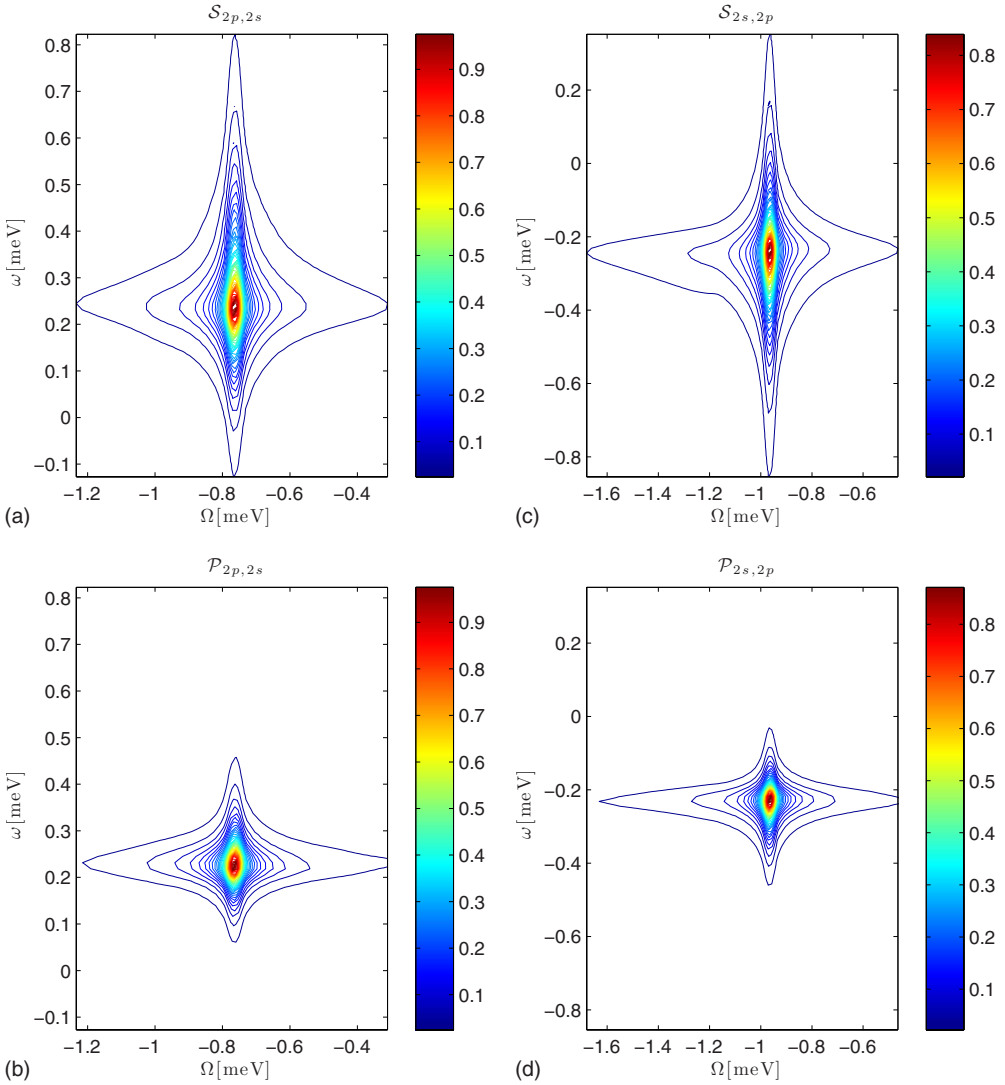

FIG. 12. (Color online) Two-dimensional plots showing absolute value of $\mathcal{S}_{2p,2s}$ and $\mathcal{P}_{2p,2s}$ at density $n_c=2\times10^{-3}a_0^{-2}$.

notation defined below Eq. (15) in the text. Arranging this matrix such that the branch indices of arguments 1 and 2 vary along rows and those of 3 and 4 along columns, it follows that for $t>t'$, all rows of $\hat{\boldsymbol{G}}_X(tt')$ are identical and given by

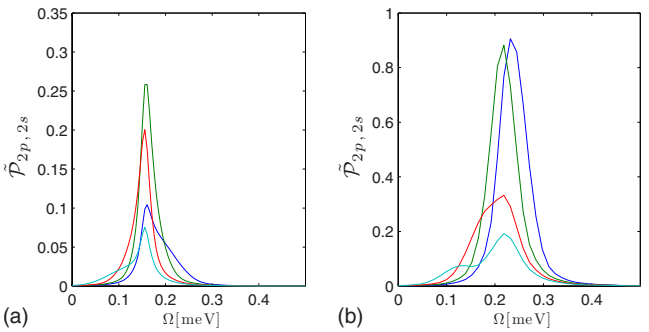

FIG. 13. (Color online) Profiles of the peaks along Ω at both densities (10^{-3} on the left and 2×10^{-3} on the right).

$$\mathcal{G}(tt') \equiv [\mathcal{G}^{>}(tt') \quad \hat{\mathcal{G}}^{-}(tt') \quad \hat{\mathcal{G}}^{+}(tt') \quad \mathcal{G}^{<}(tt')]. \tag{B2}$$

For $t<t'$, all columns are identical and given by

$$\overline{\mathcal{G}}(tt') = \begin{bmatrix} \mathcal{G}^{<}(tt') \\ \check{\mathcal{G}}^{+}(tt') \\ \check{\mathcal{G}}^{-}(tt') \\ \mathcal{G}^{>}(tt') \end{bmatrix}. \tag{B3}$$

Here, we have defined six new functions. The *lesser* and *greater* functions,

$$\mathcal{G}^{>}(tt') = -\langle a_v^{\dagger}(t)a_c(t)a_c^{\dagger}(t')a_v(t')\rangle,$$

$$\mathcal{G}^{<}(tt') = -\langle a_c^{\dagger}(t')a_v(t')a_v^{\dagger}(t)a_c(t)\rangle,$$

have equal-time operators placed together and thus they are sensitive only to the atomic nature of the exciton (see I for definition of $\langle\cdot\rangle$). The next two functions account for the composite nature of the exciton

$$\hat{\mathcal{G}}^{-}(tt') = \langle a_c^\dagger(t')a_c(t)a_v^\dagger(t)a_v(t')\rangle,$$

$$\hat{\mathcal{G}}^{+}(tt') = \langle a_v(t')a_v^\dagger(t)a_c(t)a_c^\dagger(t')\rangle,$$

$$\check{\mathcal{G}}^{-}(tt') = \langle a_v^\dagger(t)a_v(t')a_c^\dagger(t')a_c(t)\rangle,$$

$$\check{\mathcal{G}}^{+}(tt') = \langle a_c(t)a_c^\dagger(t')a_v(t')a_v^\dagger(t)\rangle.$$

The superscripts $\pm$ on these functions do not stand for the contour index. Rather, they signify the fact that $\mathcal{G}^{\pm}$ represent the annihilation of the electron-hole pair at time t in a state that evolves from $N\pm 1$ particle state at time t'. This is in contrast to the functions $\mathcal{G}^{\gtrless}$ the Lehmann representations of which are described by states only within the N-particle Hilbert space. Exploiting the equal-time anticommutation relation $\{a_c^\dagger(t), a_v(t)\}=0$, it can be verified that the equalities between Keldysh components of G carry over to $X^{(2)}$ as well. Thus, the matrix $\hat{\boldsymbol{X}}^{(2)}$ has identical rows,

$$\mathcal{X}(tt') = [\mathcal{P}^{>}(tt') \quad \hat{\mathcal{P}}^{-}(tt') \quad \hat{\mathcal{P}}^{+}(tt') \quad \mathcal{P}^{<}(tt')], \tag{B4}$$

for $t>t'$, and identical columns,

$$\overline{\mathcal{X}}(tt') = \begin{bmatrix} \mathcal{P}^{<}(tt') \\ \check{\mathcal{P}}^{+}(tt') \\ \check{\mathcal{P}}^{-}(tt') \\ \mathcal{P}^{>}(tt') \end{bmatrix}, \tag{B5}$$

for $t<t'$. As with the Green's functions above, the functions $\mathcal{P}^{\gtrless}(t,t')$ treat exciton as an indivisible particle, coupling only to its multipole moments. Besides being related to the evolution in $N\pm 1$ particle Hilbert space, the functions $\hat{\mathcal{P}}^{\pm}$ and $\check{\mathcal{P}}^{\pm}$ may also be seen as being sensitive to the individual propagation of the electron and the hole, as is clear from the operator ordering in the corresponding Green's function.

As discussed in the text, we make further approximations to close the equations of motion within the space of two-time functions. To formulate them mathematically, we begin with the semigroup property obeyed by noninteracting Green's functions

$$G_0^r(tt') = iG_0^r(tt'')G_0^r(t''t'), \tag{B6}$$

$$G_0^a(tt') = -iG_0^a(tt'')G_0^a(t''t'). \tag{B7}$$

Note that no integration is performed over the time variables, but all other degrees of freedom are summed using the matrix notation. The two-time limit is constructed by constructing the analog of semigroup property of the ideal single-particle Green's functions, which holds approximately for the full Green's functions[23,28,29]

$$G^r(tt') \approx iG^r(tt'')G^r(t''t'), \tag{B8}$$

$$G^a(tt') \approx -iG^a(tt'')G^a(t''t'). \tag{B9}$$

The "≈" here denotes the neglect of all those diagrams where the time t'' lies inside at least one self-energy insertion. This is seen from the diagrammatic expansion of Dyson equation, in which we start with G_0, pick a time t', and apply the properties (B6) and (B7). Then we dress each of the two G_0 with self-energy insertions and reject all those diagrams that cannot be cut at t' by only cutting a propagator.

Substituting the approximate Eqs. (B8) and (B9) in the Dyson equation in turn implies

$$G^{<}(tt') \approx \begin{cases} iG^r(tt'')G^{<}(t''t') & t>t''>t' \\ -iG^{<}(tt'')G^a(t''t') & t<t''<t'. \end{cases}$$

Collecting these functions in the matrix form and transforming back to the contour indices, we get

$$\hat{G}(tt') = \begin{cases} i\hat{G}(tt'')\sigma^z\hat{G}(t''t') & t>t''>t' \\ -i\hat{G}(tt'')\sigma^z\hat{G}(t''t') & t<t''<t'. \end{cases}$$

APPENDIX C: DERIVATION OF EOM

1. Derivation of two-particle EOM

For brevity, we show how to write the $J_{\mathrm{Q}}\mathfrak{X}_2^{(2)}$ part of Eq. (17) using the Keldysh matrix representation, with the special structure [Eqs. (B4) and (B5)]. The $J_2X_{\mathrm{Q}}^{(2)}$ term is obtained analogously.

To proceed, we write the interaction part of the equation as

$$\hat{\boldsymbol{I}}(tt';t^+t'^+) = \int \hat{\boldsymbol{J}}_{\mathrm{Q}}(tt'';t^+t''^+)\hat{\boldsymbol{Z}}\hat{\boldsymbol{P}}(t''t';t''^+t'^+)dt'',$$

where

$$\hat{\boldsymbol{Z}} = \begin{bmatrix} 1 & & & \\ & -1 & & \\ & & -1 & \\ & & & 1 \end{bmatrix}.$$

To further simplify this, we divide the integration over t'' into three regions

$$\hat{\boldsymbol{I}}^{(1)}_{cvvc}(tt';t^+t'^+) = \int_{t_{min}}^{t_{max}} \hat{\boldsymbol{J}}_{\mathrm{Q};cvvc}(tt'';t^+t''^+)\hat{\boldsymbol{Z}}\hat{\boldsymbol{P}}(t''t';t''^+t'^+)dt'',$$

$$\hat{\boldsymbol{I}}^{(2)}_{cvvc}(tt';t^+t'^+) = \int_{t_{max}}^{\infty} \hat{\boldsymbol{J}}_{\mathrm{Q};cvvc}(tt'';t^+t''^+)\hat{\boldsymbol{Z}}\hat{\boldsymbol{P}}(t''t';t''^+t'^+)dt'',$$

$$\hat{\boldsymbol{I}}^{(3)}_{cvvc}(tt';t^+t'^+) = \int_{-\infty}^{t_{min}} \hat{\boldsymbol{J}}_{\mathrm{Q};cvvc}(tt'';t^+t''^+)\hat{\boldsymbol{Z}}\hat{\boldsymbol{P}}(t''t';t''^+t'^+)dt''.$$

where $t_{min}=\min(t,t')$ and $t_{max}=\max(t,t')$. For $t>t'$, we obtain

$$\mathcal{I}^{(1)}_{cvvc}(tt') = \int_{t'}^{t} \mathcal{J}^r_{\mathrm{Q};cvvc}(tt'')\mathcal{P}(t''t')dt'',$$

$$\mathcal{I}^{(2)}_{cvvc}(tt') = 0,$$

$$\mathcal{I}^{(3)}_{cvvc}(tt') = \int_{-\infty}^{t'} \mathcal{J}_{\mathrm{Q}}(tt'')\hat{\mathbf{Z}}\overline{\mathcal{P}}(t''t')dt''.$$

Here, $\mathcal{I}^{(j)}$ are the row vectors of the same form as $\mathcal{P}$ with the corresponding elements. From the properties of $\mathcal{J}$, it also follows that

$$\sum_{\sigma\sigma'} \sigma\sigma' \mathcal{I}^{(3)\sigma\gamma\sigma'\gamma'}_{\mathrm{Q};cvvc}(tt') = 0.$$

In the equation for $\mathcal{P}^<$, it is $\mathcal{I}^<$ that contributes. In the two regimes, $t>t'$ and $t<t'$, it is

$$\mathcal{I}^<(tt') = \int_{t'}^{t} dt'' \mathcal{J}^r_{\mathrm{Q}}(tt'')\mathcal{P}^<(t''t') + i\int_{-\infty}^{t'} \mathcal{J}_{\mathrm{Q}}(tt'')\hat{\mathbf{Z}}\overline{\mathcal{P}}(t''t')dt'', \quad t>t',$$

$$\mathcal{I}^<(tt') = \int_{t}^{t'} dt'' \overline{\mathcal{J}}_{\mathrm{Q}}(tt'')\mathcal{P}^a(t''t') + i\int_{-\infty}^{t} \mathcal{J}_{\mathrm{Q}}(tt'')\hat{\mathbf{Z}}\overline{\mathcal{P}}(t''t')dt'', \quad t<t'.$$

By expanding the last term into a sum over its components, we obtain

$$\mathcal{I}^<(tt')\theta(t-t') + \mathcal{I}^<(tt')\theta(t'-t) = i\int_{t_{min}}^{t_{max}} \mathcal{J}^r_{\mathrm{Q}}(tt'')\mathcal{P}^<(t''t') + \mathcal{J}^<_{\mathrm{Q}}(tt'')\mathcal{P}^a(t''t') + i\int_{-\infty}^{t_{min}} \mathcal{J}^<_{\mathrm{Q}}(tt'')\mathcal{P}^>(t''t') + \mathcal{J}^>_{\mathrm{Q}}(tt'')\mathcal{P}^<(t''t')dt'' - i\int_{-\infty}^{t_{min}} \hat{\mathcal{J}}_{\mathrm{Q}}(tt'')\check{\mathcal{P}}^+(t''t') + \hat{\mathcal{J}}^+_{\mathrm{Q}}(tt'')\check{\mathcal{P}}^-(t''t')dt'', \tag{C1}$$

where $t_{min}=\min(t,t')$ and $t_{max}=\max(t,t')$. Similar steps lead to an expression, in terms of the Keldysh components, for the term $J_2X^{(2)}_{\mathrm{Q}}$ in Eq. (17). After restoring the $\sigma(11'')$ and $\sigma(1''4)$ in Eq. (17) as discussed just above that equation and adding $J_{\mathrm{Q}}\mathfrak{X}^{(2)}_2$ and $J_2X^{(2)}_{\mathrm{Q}}$ terms, we obtain Eq. (38) in Sec. IV.

2. Derivation of single-particle EOM

We now derive an expression for the interband polarization by using the semigroup approximation, which is the same as generalized Kadanoff Baym ansatz (GKBA) in this case. We will consider the dynamically screened Hartree-Fock self-energy with a vertex correction arising from electron-hole interaction. From the Dyson equation, the "+ −" Keldysh components of the couplings in Eq. (12) are

$$\mathcal{M}^{(11;1)}_1\mathfrak{X}^{(1)}_1 = \Sigma^s_{\mathrm{Q}cc}(\boldsymbol{k},t_1)\mathfrak{X}^{+-}_{1;cv}(\boldsymbol{k}|t_1t_2), \tag{C2}$$

$$\mathcal{M}^{(12;1)}_1\mathfrak{X}^{(2)}_1 = iW^{+\sigma}_{\mathrm{Q}}(\boldsymbol{q}|t-t')\{\mathfrak{X}^{+\sigma;-\sigma}_{1;cvvv}(\boldsymbol{k},\boldsymbol{k}',\boldsymbol{q}|tt';t^+t'^+) + \mathfrak{X}^{+\sigma;-\sigma}_{1;ccvc}(\boldsymbol{k},\boldsymbol{k}',\boldsymbol{q}|tt';t^+t'^+)\}. \tag{C3}$$

We obtained these by separating the self-energy into the static part Σ^s and a purely dynamical part Σ and we have indicated the first-order variation in the self-energy by superscript "1." The above formula gives $\mathcal{M}^{(12;1)}_1$ [Eq. (12)] since it is coupled to the functions $\mathfrak{X}_{1;cvvv}$ and $\mathfrak{X}_{1;ccvc}$.

We now employ the GKBA (Ref. 30) in the form

$$\mathfrak{X}^{+-}_{1;cv}(12) = \mathfrak{X}^{-+}_{1;cv}(12) = \mathfrak{X}^{+-}_{1;cv}(1)G^a_{vv}(12) - G^r_{cc}(12)\mathfrak{X}^{+-}_{1;cv}(2),$$

$$\mathfrak{X}^{++}_{1;cv}(12) = \mathfrak{X}^{--}_{1;cv}(12) = \mathfrak{X}^{+-}_{1;cv}(1)G^a_{vv}(12) - G^r_{cc}(12)\mathfrak{X}^{+-}_{1;cv}(2).$$

Note that all $O(U)$ components of the Keldysh matrix for G_{cv} are equal and this is due to the anticommutation relation $\{a_{v\boldsymbol{k}},a_{c\boldsymbol{k}}\}=\{a_{v\boldsymbol{k}},a^\dagger_{c\boldsymbol{k}}\}=0$. We apply GKBA to approximate $\mathfrak{X}_{1;cvvv}$ and $\mathfrak{X}_{1;ccvc}$ functions by a product of particle-conserving exciton correlation $\mathfrak{X}_{1;cvvc}$ and the interband polarization as follows:

$$\mathfrak{X}^{(2)+\sigma-\sigma}_{1;cvvv}(\boldsymbol{k},\boldsymbol{k}',\boldsymbol{q}|tt';tt') = -X^{(2)+\sigma-\sigma}_{\mathrm{Q};cvvc}(\boldsymbol{k},\boldsymbol{k}',\boldsymbol{q}|tt';tt')\mathfrak{X}^{\sigma\sigma}_{1;cv}(\boldsymbol{k}',t';\boldsymbol{k}'t'), \tag{C4}$$

$$\mathfrak{X}^{(2)+\sigma-\sigma}_{1;ccvc}(\boldsymbol{k},\boldsymbol{k}',\boldsymbol{q}|tt';tt') = X^{(2)+\sigma-\sigma}_{\mathrm{Q};cvvc}(\boldsymbol{k},\boldsymbol{k}',\boldsymbol{q}|tt';tt')\mathfrak{X}^{\sigma\sigma}_{1;cv}(\boldsymbol{k}'+\boldsymbol{q},t';\boldsymbol{k}'+\boldsymbol{q},t'). \tag{C5}$$

This approximation is most easily understood diagrammatically by directly performing vertex corrections corresponding to electron-hole interaction in the Hartree-Fock self-energy.

Combining Eqs. (C3) and (C2) with their adjoint, imposing the GKBA, setting $t_1=t_2=t$, and writing $\mathfrak{X}^{+-}_{cv}(tt)=i\rho_{cv}(t)$ for brevity, we get

$$\left(\frac{\partial}{\partial t} + i\omega_{c\boldsymbol{k}}\right)\rho_{cv}(\boldsymbol{k},t) - iU_{cv}(\boldsymbol{k}t;\boldsymbol{k}t^+)\{f_{v\boldsymbol{k}}-f_{c\boldsymbol{k}}\} - \Sigma^s_{\mathrm{Q}cc}(\boldsymbol{k},t)\rho_{cv}(\boldsymbol{k},t) = \{f_{v\boldsymbol{k}}-f_{c\boldsymbol{k}}\}\int \frac{d\boldsymbol{k}'}{4\pi^2}V^s(\boldsymbol{k}-\boldsymbol{k}')\rho_{cv}(\boldsymbol{k}',t) + \int dt'\int \frac{d\boldsymbol{q}}{4\pi^2} iW^{+\sigma}_{\mathrm{Q}}(\boldsymbol{q}|t-t')\int \frac{d\boldsymbol{k}d\boldsymbol{k}'}{16\pi^4}\{\mathfrak{X}^{(2)+\sigma-\sigma}_{1;cvvv}(\boldsymbol{k},\boldsymbol{k}',\boldsymbol{q}|tt';tt') + \mathfrak{X}^{(2)+\sigma-\sigma}_{1;ccvc}(\boldsymbol{k},\boldsymbol{k}',\boldsymbol{q}|tt';tt')\} - \int dt'\int \frac{d\boldsymbol{q}}{4\pi^2} iW^{\sigma-}_{\mathrm{Q}}(\boldsymbol{q}|t'-t)\int \frac{d\boldsymbol{k}d\boldsymbol{k}'}{16\pi^4}\{\mathfrak{X}^{(2)+\sigma-\sigma}_{1;cvvv}(\boldsymbol{k}-\boldsymbol{q},\boldsymbol{k}',\boldsymbol{q}|tt';tt') + \mathfrak{X}^{(2)+\sigma-\sigma}_{1;ccvc}(\boldsymbol{k}-\boldsymbol{q},\boldsymbol{k}',\boldsymbol{q}|tt';tt')\}. \tag{C6}$$

Here, V^s is the static part of screened interaction. We have not yet substituted Eqs. (C4) and (C5), but will do so when projecting this equation onto the exciton basis using Eq. (25). The condition of zero-exciton density in equilibrium when applied to the last two terms in Eq. (C6) allows only the positive contour index, i.e., $\sigma=+$. With $\sigma=-$, there is always at least one occurrence of $G^>_{\mathrm{Q}vv}$, which vanishes. To project Eq. (C6) onto the exciton basis, we substitute Eqs. (C4) and (C5) and integrate them over $\boldsymbol{k}$ and $\boldsymbol{k}'$ as follows:

$$\int \frac{d\boldsymbol{k}}{4\pi^2}\varphi_n^*(\boldsymbol{k})\int \frac{d\boldsymbol{k}'}{4\pi^2}\mathfrak{X}^{++-+}_{1cvvv}(\boldsymbol{k},\boldsymbol{k}',\boldsymbol{q}|tt';tt') + \mathfrak{X}^{++-+}_{1ccvc}(\boldsymbol{k},\boldsymbol{k}',\boldsymbol{q}|tt';tt') = -\sum_{jm}\mathcal{P}^{>}_{\mathbb{Q}jj}(tt')\rho_m(t')\int \frac{d\boldsymbol{k}}{4\pi^2}\varphi_n^*(\boldsymbol{k})\varphi_j(\boldsymbol{k}+\alpha_c\boldsymbol{q})\int \frac{d\boldsymbol{k}'}{4\pi^2}\{\varphi_j^*(\boldsymbol{k}'-\alpha_v\boldsymbol{q})\varphi_m(\boldsymbol{k}') - \varphi_j^*(\boldsymbol{k}'-\alpha_v\boldsymbol{q})\varphi_m(\boldsymbol{k}'+\boldsymbol{q})\} = \sum_{jm} O_{nj}(\boldsymbol{0},\alpha_c\boldsymbol{q})A_{jm}(\boldsymbol{q})\mathcal{P}^{>}_{\mathbb{Q}jj}(tt')\rho_m(t'),$$

where $A(\boldsymbol{q})=A(\boldsymbol{0},\boldsymbol{q})$ [see discussion below Eq. (45) in text]. To obtain the last line, we have used the relation $\alpha_c=1+\alpha_v$ in the integral over $\boldsymbol{k}'$,

$$\int \frac{d\boldsymbol{k}'}{4\pi^2}\varphi_j^*(\boldsymbol{k}'-\alpha_v\boldsymbol{q})\varphi_m(\boldsymbol{k}'+\boldsymbol{q}) = \int \frac{d\boldsymbol{k}'}{4\pi^2}\varphi_j^*(\boldsymbol{k}')\varphi_m[\boldsymbol{k}'+(1+\alpha_v)\boldsymbol{q}] = O_{jm}(\boldsymbol{0},\alpha_c\boldsymbol{q}).$$

The integrals in the last term of Eq. (C6) are handled similarly, obtaining

$$\int \frac{d\boldsymbol{k}}{4\pi^2}\varphi_n^*(\boldsymbol{k})\int d\boldsymbol{k}'\,\mathfrak{X}^{++-+}_{1cvvv}(\boldsymbol{k}-\boldsymbol{q},\boldsymbol{k}',\boldsymbol{q}|tt';tt') + \mathfrak{X}^{++-+}_{1ccvc}(\boldsymbol{k}-\boldsymbol{q},\boldsymbol{k}',\boldsymbol{q}|tt';tt') = -\sum_{jm}\mathcal{P}^{>}_{\mathbb{Q}jj}(tt')\rho_m(t')\int \frac{d\boldsymbol{k}}{4\pi^2}\varphi_n^*(\boldsymbol{k})\varphi_j(\boldsymbol{k}-\alpha_v\boldsymbol{q})\int \frac{d\boldsymbol{k}'}{4\pi^2}\{\varphi_j^*(\boldsymbol{k}'-\alpha_v\boldsymbol{q})\varphi_m(\boldsymbol{k}') - \varphi_j^*(\boldsymbol{k}'-\alpha_v\boldsymbol{q})\varphi_m(\boldsymbol{k}'+\boldsymbol{q})\} = \sum_{jm} O_{nj}(\boldsymbol{0},-\alpha_v\boldsymbol{q})A(\boldsymbol{q})\mathcal{P}^{>}_{\mathbb{Q}jj}(tt')\rho_m(t').$$

The differential equation now takes the form

$$\left(\frac{\partial}{\partial t}+i\omega_n\right)\rho_n(t) - U_n(t) = \sum_{jm}\int dt''\int \frac{d\boldsymbol{q}}{4\pi^2} iW^{<}_{\mathbb{Q}}(\boldsymbol{q},\tau)\times\{O_{nj}(\boldsymbol{0},\alpha_c\boldsymbol{q}) - O_{nj}(\boldsymbol{0},\alpha_v\boldsymbol{q})\}A_{jm}(\boldsymbol{q})\mathcal{P}^{>}_{\mathbb{Q}jj}(\tau)\rho_m(t-\tau) = \sum_m \int dt''\left\{\sum_j \int \frac{d\boldsymbol{q}}{4\pi^2} iW^{<}_{\mathbb{Q}}(\boldsymbol{q},-\tau)A_{nj}(\boldsymbol{q})A_{jm}(\boldsymbol{q})\mathcal{P}^{>}_{\mathbb{Q}jj}(\tau)\right\}\rho_m(t-\tau) = \sum_m \int dt''\mathcal{B}_{nm}(\tau)\rho_m(t-\tau).$$

In the last equality, we have used the definition (44) of the matrix $\mathcal{B}(\tau)$, while on the left-hand side we have combined the coulomb interaction terms and the band energies into the exciton energy levels, $\hbar\omega_n$. The projection of $iU_{cv}(\boldsymbol{k}t;\boldsymbol{k}t^+)\{f_{v\boldsymbol{k}}-f_{c\boldsymbol{k}}\}$ on the exciton states is denoted by $U_n(t)$. Thus, the single-particle equation takes the form shown in Eq. (42) or (47).

3. Expressions for interaction matrix components

After several algebraic steps starting from the expression (16) defined on the Keldysh contour, the expressions for the components of $\mathcal{J}_{\boldsymbol{q}}$ are as follows:

$$\mathcal{J}^{>}_{\boldsymbol{q}}(tt') = -i\int \frac{d\boldsymbol{q}'}{4\pi^2}W^{>}(\boldsymbol{q}-\boldsymbol{q}'|tt')A(\boldsymbol{q},\boldsymbol{q}')\mathcal{P}^{>}_{\boldsymbol{q}'}(tt')A(\boldsymbol{q}',\mathbf{q}),$$

$$\mathcal{J}^{<}_{\boldsymbol{q}}(tt') = -i\int \frac{d\boldsymbol{q}'}{4\pi^2}W^{<}(\boldsymbol{q}-\boldsymbol{q}'|tt')A(\boldsymbol{q},\boldsymbol{q}')\mathcal{P}^{<}_{\boldsymbol{q}'}(tt')A(\boldsymbol{q}',\boldsymbol{q}).$$

While we mainly work with these components in the text, we also give expressions for the rest for completeness

$$\hat{\mathcal{J}}_{\boldsymbol{q}}(tt') = -i\int \frac{d\boldsymbol{q}'}{4\pi^2}W^{<}(\boldsymbol{q}-\boldsymbol{q}'|tt')A(\boldsymbol{q},\boldsymbol{q}')\hat{\mathcal{P}}^{-}_{\boldsymbol{q}-\boldsymbol{q}'}(tt')A(\boldsymbol{q}') - \frac{1}{2}[iW^{<}(\boldsymbol{q}-\boldsymbol{q}'|tt') - iW^{>}(\boldsymbol{q}-\boldsymbol{q}'|tt')]F(\boldsymbol{q}')\hat{\mathcal{P}}^{-}_{\boldsymbol{q}'}(tt')A(\boldsymbol{q}',\boldsymbol{q}),$$

$$\hat{\mathcal{J}}^{+}_{\boldsymbol{q}}(tt') = -i\int \frac{d\boldsymbol{q}'}{4\pi^2}W^{>}(\boldsymbol{q}-\boldsymbol{q}'|tt')A(\boldsymbol{q},\boldsymbol{q}')\hat{\mathcal{P}}^{+}_{\boldsymbol{q}'}(tt')A(\boldsymbol{q}',\boldsymbol{q}) - \frac{1}{2}[iW^{>}(\boldsymbol{q}-\boldsymbol{q}'|tt') - iW^{<}(\boldsymbol{q}-\boldsymbol{q}'|tt')]F(\boldsymbol{q},\boldsymbol{q}')\hat{\mathcal{P}}^{+}_{\boldsymbol{q}'}(tt')A(\boldsymbol{q}',\boldsymbol{q}),$$

$$\check{\mathcal{J}}^{+}_{\boldsymbol{q}}(tt') = i\int \frac{d\boldsymbol{q}'}{4\pi^2}W^{<}(\boldsymbol{q}-\boldsymbol{q}'|tt')A(\boldsymbol{q},\boldsymbol{q}')\check{\mathcal{P}}^{+}_{\boldsymbol{q}'}(tt')A(\boldsymbol{q}',\boldsymbol{q}) + \frac{1}{2}[iW^{<}(\boldsymbol{q}-\boldsymbol{q}'|tt') - iW^{>}(\boldsymbol{q}-\boldsymbol{q}'|tt')]A(\boldsymbol{q},\boldsymbol{q}')\check{\mathcal{P}}^{+}_{\boldsymbol{q}'}(tt')F(\boldsymbol{q}',\boldsymbol{q})$$

$$\check{\mathcal{J}}^{-}_{\boldsymbol{q}}(tt') = i\int \frac{d\boldsymbol{q}'}{4\pi^2}W^{>}(\boldsymbol{q}-\boldsymbol{q}'|tt')A(\boldsymbol{q},\boldsymbol{q}')\check{\mathcal{P}}^{-}_{\boldsymbol{q}'}(tt')A(\boldsymbol{q}',\boldsymbol{q}) + \frac{1}{2}[iW^{>}(\boldsymbol{q}-\boldsymbol{q}'|tt') - iW^{<}_{\mathbb{Q}}(\boldsymbol{q}-\boldsymbol{q}'|tt')]A(\boldsymbol{q},\boldsymbol{q}')\check{\mathcal{P}}^{-}_{\boldsymbol{q}'}(tt')F(\boldsymbol{q}',\boldsymbol{q}).$$

Note that only the matrix A appears in expressions for $\mathcal{J}^{\lessgtr}$, which are sensitive only to the multipole moments of the exciton. On the other hand, the composite functions always contain a contribution from F,

$$F_{nm}(\boldsymbol{q},\boldsymbol{q}') \equiv O_{nm}(\alpha_c\boldsymbol{q},\alpha_c\boldsymbol{q}') + O_{nm}(\alpha_v\boldsymbol{q},\alpha_v\boldsymbol{q}'),$$

which is sensitive to the states of the electron and hole individually. Since we have neglected the latter functions, the equation we obtain is entirely in terms of A.

*kvirk@physics.utoronto.ca
†sipe@physics.utoronto.ca

[1] F. Rossi, S. Haas, and T. Kuhn, Phys. Rev. Lett. **72**, 152 (1994).
[2] V. L. Gurevich, M. I. Muradov, and D. A. Parshin, EPL **12**, 375 (1990).
[3] P. C. Becker, H. L. Fragnito, C. H. Brito Cruz, R. L. Fork, J. E. Cunningham, J. E. Henry, and C. V. Shank, Phys. Rev. Lett. **61**, 1647 (1988).
[4] W. A. Hügel, M. F. Heinrich, M. Wegener, Q. T. Vu, L. Bányai, and H. Haug, Phys. Rev. Lett. **83**, 3313 (1999).
[5] M. Lindberg, R. Binder, and S. W. Koch, Phys. Rev. A **45**, 1865 (1992).
[6] L. Schultheis, M. D. Sturge, and J. Hegarty, Appl. Phys. Lett. **47**, 995 (1985).
[7] R. D. R. Bhat and J. E. Sipe, Phys. Rev. Lett. **85**, 5432 (2000).
[8] H. van Driel and J. Sipe, *Coherent Control of Photocurrents in Semiconductors* (Springer, New York, 1999), Chap. 5, p. 261.
[9] I. Kuznetsova, P. Thomas, T. Meier, T. Zhang, X. Li, R. Mirin, and S. Cundiff, Solid State Commun. **142**, 154 (2007).
[10] X. Li, T. Zhang, C. N. Borca, and S. T. Cundiff, Phys. Rev. Lett. **96**, 057406 (2006).
[11] L. Yang, I. V. Schweigert, S. T. Cundiff, and S. Mukamel, Phys. Rev. B **75**, 125302 (2007).
[12] K. S. Virk and J. E. Sipe, preceding paper, Phys. Rev. B **80**, 165318 (2009).
[13] K. B. Ferrio and D. G. Steel, Phys. Rev. Lett. **80**, 786 (1998).
[14] Here, $\varepsilon^{-1}(3'4;4'3)$, which is the inverse dielectric function that transforms the response to effective field into the response to the external field, should multiply $X^{(2)}$. We do not display it here because in Eq. (6), we set $\varepsilon^{-1}_{\zeta_{3'v};\zeta_{4'c}}(3'4;4'3)$ equal to unity. This approximation neglects the matrix elements of Coulomb interaction across the fundamental gap, as well as the effects on the response due to the motion of carriers perpendicular to the plane of the quantum well.
[15] P. Kral and J. Sipe, Phys. Rev. B **61**, 5381 (2000).
[16] In the following sections, we discuss the set of physical and mathematical approximations within which this correlation function alone captures the entire TDFS signal generated by Raman coherence among exciton states.
[17] We also argue in Sec. IV that EID makes only a quantitative difference in the type of decoherence studied.
[18] The diagrams that contribute to this coupling inevitably contain at least one G_{Q} line from negative to the positive contour, which as discussed in I is proportional to density.
[19] The most general form for $I^{(2)}$ is displayed diagrammatically in Figs. I-6(a)–I-6(c).
[20] K. Virk, Ph.D. thesis, University of Toronto, 2009).
[21] Doing so would be inconsistent with the left-hand side because, in the full diagram, the pair of propagators is $G_{cv}G_{cc}$ or $G_{vv}G_{vc}$, etc. It would also be inconsistent because it would modify the effective interaction in such a way that it would include both pulses, which is a second-order deviation that should be in the dynamical map and not the source term.
[22] We will continue using "Q" explicitly when a function is to be evaluated at equilibrium.
[23] T. Bornath, D. Kremp, and M. Schlanges, Phys. Rev. E **60**, 6382 (1999).
[24] P. Martin and J. Schwinger, Phys. Rev. **115**, 1342 (1959).
[25] R. Zimmermann, *Many-Particle Theory of Highly Excited Semiconductors* (Teubner, Leipzig, 1988).
[26] J. Negele, *Quantum Many-Particle Systems* (Addison-Wesley Publishing Company, Reading, MA, 1988).
[27] P. Linz, *Analytical and Numerical Methods for Volterra Equations* (SIAM, Philadelphia, 1985).
[28] B. Velicky, A. Kalvova, and V. Spicka, Phys. Rev. B **75**, 195125 (2007).
[29] B. Velický, A. Kalvová, and V. Špička, Phys. Rev. B **77**, 041201(R) (2008).
[30] W. Schafer and M. Wegener, *Semiconductor Optics and Transport Phenomena* (Springer, Berlin, 2001).